Computer Generated Holograms Applied to Optical Tweezers

By

Ulises Ruiz Corona

A dissertation submitted to the program in Optics of the Optics Department in partial fulfillment of the requirements for the degree of

Doctor in Optics

At the

National Institute for Astrophysics, Optics and Electronics

Advisors:

Dr. Víctor Manuel Arrizón Peña

Dr. Rubén Ramos García

INAOE

September 2009

Sta. Maria Tonantzintla, Puebla

INSTITUTO NACIONAL DE ASTROFISICA, OPTICA Y ELECTRONICA

Computer Generated Holograms Applied to Optical Tweezers

A thesis presented
by

Ulises Ruiz Corona

to

The Department of Optics
in partial fulfillment of the requirements
for the degree of

Doctor of Philosophy

in the subject of

Optica

Sta. Maria Tonantzintla, Puebla

September 2009

[You may place a comment here.]

Acknowledgments

I would like to thank my family for their support and understanding during the development of this work. I would also like to thank my supervisors Dr. Víctor Manuel Arrizón Peña, and Dr. Rubén Ramos García for their guidance and the knowledge taugh to me, which was the most important factor to obtain the results. I would like to thanks all judge members: Dra. Karen Patricia Volke Sepulveda, Dra. Svetlana Mansurova, Dr. Víctor Ruiz Cortes, Dr. David Sánchez de la Llave, and Dr. Julio Cesar Ramírez San Juan for reading this thesis. My thanks also extend to Dr. Carlos Gerardo Treviño Palacios, who allowed us use the laser to obtain some results reported.

Thanks also go to my friends, who help me and allowed that the staying at the INAOE was a very good experience.

Finally I would like to thank CONACYT for the financial support.

Contents

Introduction

The word holography is a combination of two Greek words: holos meaning "whole", and graphein meaning "to write". Thus, holography means writing or recording of 3D information, i.e., amplitude and phase of a wavefront [2].

The fundamental theory of wavefront reconstruction or holography was developed by Gabor [1]. He also showed that a 3D object could be reconstructed through wavefront reconstruction. Gabor combine two mutually coherent co-propagating object and reference beams, he was able to record a 3D object field onto a photographic plate (hologram). This type of hologram is known as an on-axis hologram or simply the Gabor hologram, by which the object and reference beams are directly impinging on the recording medium in the same direction [2].

The concept of holographic imaging received little attention until the discovery of the laser in the early 1960s [3]. In 1962, Leith and Upatniek [4] used an oblique instead of an on-axis reference beam. They were able to record holograms with high-contrast fringes using a laser source. It was the first time that a 3D high-quality holographic image was observed [2]. The Off-axis holograms, also known as spatial carrier frequency holograms (or simply the Leith holograms), allowed to separate the image and noise better than the Gabor holograms.

Also in 1962, Denisyuk adapted Lippmann's technique [5] by combining a set of counterpropagating object and reference beams to record holograms in a thick emul-

sion photographic plate [6]. These kind of holograms are called reflection holograms or simply the Denisyuk holograms.

To record these holograms, it was necessary to have physically the object to codify. In 1966 A. W. Lohmann revolutionized the holography through the invention of the computer generated holograms (CGHs), which can create wavefronts that may be defined only mathematically eliminating the need of physical objects [7]. The first CGHs were binaries; they consisted of many transparent dots on an opaque background. To produce these CGHs, the holograms were plotted first in black and white on a large scale, later they were optically reduced in size and recorded on a photographic film [8].

Although the binary CGHs were easy to record on a film, the quality of the reconstructed image was poor. Therefore, in 1970 Lee [9] developed the 256 gray levels CGHs. This quantization of the gray levels allowed better quality than the Lohmann's binary hologram. With the improvement of CGHs, the applications have increased enormously; the CGHs have been used for example: to generate spatial frequency filters [10], to test aspheric wavefronts [11], to correct aberrations [12], to generate nondiffracting beams [13], in beam shaping [14], to mention just a few applications.

The CGHs can be classified in two types: amplitude holograms and phase holograms. In the amplitude holograms, the amplitude and phase of the wavefront to codify

are represented as an only-amplitude function, while in the phase holograms, the amplitude and phase of the wavefront to codify are represented as an only-phase function. In this thesis the central topic of discussion will be the phase holograms because this type of holograms offer higher diffraction efficiency since absorption of light is minimum reducing undesirable heating on high power applications.

As it was described above, the method to create the transparency of a CGH was complex, expensive, and did not work in real time. Therefore, with the development of the spatial light modulators (SLMs) was possible replace the photographic films to record the CGHs. In recent years the use of SLMs, for CGHs, has increased because their electrical addressable pixels can provide precise, repeatable, and reconfigurable optical modulations.

The CGHs displayed on SLMs can generate complex light fields, including Bessel beams [15], Laguerre-Gauss beams [15], periodic non-diffractive fields [16], and Airy beams[17] to mention some. Also arrays of spots [18] or spatially varying optical landscapes like fringes have been denmostrated [19]. The enormous potential offered by CGHs displayed in SLMs has taken full advantage on the manipulation of microscopic objects (optical tweezers). For example projecting a sequence of CGHs is possible reconfigure the resulting pattern, and then can be manipulate dynamically a large number of microscopic objects.

In this thesis is presented the theoretical discussion and the experimental realization of two novel phase CGHs (synthetic phase holograms), that compared with others already reported in the literature [15],[20], present a better quality in the reconstructed field. Also two experimental applications of structured light patterns in optical tweezers are presented.

The content of this thesis is organized as follow, the chapter 1 describes the components and working of SLMs, the chapter 2 describes the general theory of holography, and presents the realization of two novel synthetic phase holograms that generate complex fields. These synthetic phase holograms present a good experimental reconstruction of the complex fields codified. Moreover one of these phase synthetic holograms can be implemented with a reduced phase modulation. The chapter 3 presents the basic theory of optical tweezers, the chapter 4 presents two applications of structured light patterns generated with a CGH, in optical tweezers. The first application shows the separation of different micron-sized particles using dynamical optical landscapes, the second application shows the Brownian motion rectification of microparticles based in the flashing ratchet technique. Finally the chapter 5 remarks the conclusions.

Chapter 1

Spatial Light Modulators

1.1 Introduction

The technology of photographic emulsions has a long history and is extremely well developed. However, such materials have one distinct disadvantage when image or signal processing is concerned, namely the long time delays required for chemical processing. In the event that the data to be processed is already in photographic form, this may not pose a significant problem. However, if information is being rapidly gathered, perhaps by some electronic means, is preferable to have a more direct interface between the electronic information and the data processing system. For this reason those working in the field of optical information processing have explored a large number of devices capable of converting data in electronic form into spatially modulated coherent optical signals. Such device is called a spatial light modulator (SLM) [21].

The SLMs are an useful tool in holography, due to their versatility to modulate both amplitude and phase of the light and their dynamic reconfiguration capability. The SLM system consists of a two dimensional array formed by pixels ($M \times N$) of $a \times b$ size each one, as shows the Fig. 1.1, that can be electrically addresed. Each pixel consists of a liquid crystal (LC) cell sandwiched between transparent electrodes. In the early days of SLMs, the LC cells were driven by two sets of electrodes ($M + N$) using multiplexing technique. The advantage of multiplexing is that $M \times N$ pixels can be addressed by using $M + N$ electrical contacts. The simplicity of multiplexing, however leads to a degradation of the device performance, especially in the viewing contrast and the limited pixel resolution. The performance of SLMs was later improved by using a different driving technique that involves the use of thin film transistor (TFT) arrays. In TFT arrays, each pixel is driven by a transistor. This significantly increases the performance and reduces the production cost.

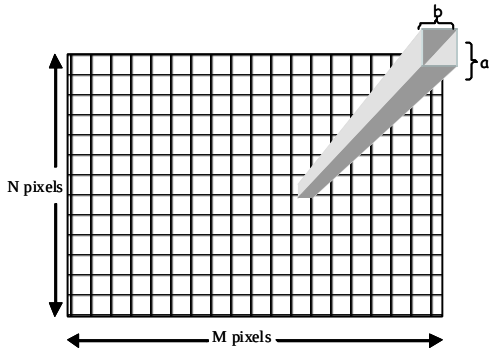

Figure 1.1. SLM system array formed by M $\times$ N of $a \times b$ size each one.

1.2 Properties of liquid crystals

Liquid crystal is a state of matter that is intermediate between the crystalline solid and the amorphous liquid. It may also be viewed as a liquid in which an ordered arrangement of molecules exists. Liquid crystals arise under certain conditions in organic substances having sharply anisotropic molecules, that is, highly elongated (rodlike) molecules or flat (disklike) molecules. A direct consequence of the ordering of the anisotropic molecules is the anisotropy of mechanical, electric, magnetic, and optical properties. This intermediate state was first observed in 1888 in cholesteryl benzoate, a crystalline solid. It becomes a turbid cloudy liquid, or liquid crystals, when heated to $145°C$; on further heating to $179°C$ the liquid becomes isotropic and clear. The sequence is reversed when the substance is cooled down. The cloudy intermediate phase contains domains that seem to have a crystal like molecular structure.

1.2.1 Liquid crystal phases

In general, there are three phases of liquid crystals, known as smetic phase, nematic phase, and cholesteric phase. For simplicity, it is assumed that the liquid crystals are made of rodlike molecules. Fig. 1.2(a) illustrates the smetic phase in which one dimensional translational order as well as orientational order exist. A unit vector $\widehat{n}$ in the direction of the preferred orientation of the molecular axes is known

as the director vector. Fig. 1.2(b) illustrates the nematic phase in which only a long range orientational order of the molecular axes exists. The cholesteric phase is also a nematic type of LC except that it is composed of chiral molecules. As a consequence, the structure acquires a spontaneous twist about a helical axis normal to the director. The twist may be right-handed or left-handed depending on the molecular chirality. Fig. 1.2(c) illustrates the cholesteric phase of LC by viewing the distribution of molecules at several planes that are perpendicular to the helical axis.

A smetic LC is closest in structure to solid crystal. It is interesting to note that in substances that form both a nematic phase and a smetic phase, the sequence of phase changes on rising temperature is as follows:

Smetic liquid crystal →Nematic liquid crystal → Cholesteric liquid crystal.

Although the smetic phase possesses the highest degree of order, the nematic and cholesteric phases have the greatest number of electrooptical applications. In the nematic phase, the medium may appear milky if the orientation order exist in many different domains. The nematic liquid crystal is clear only when a long range order exists in the whole medium. At the nematic isotropic transition temperature, the medium becomes isotropic and looks clear and transparent. This temperature is also known as the clearing point.

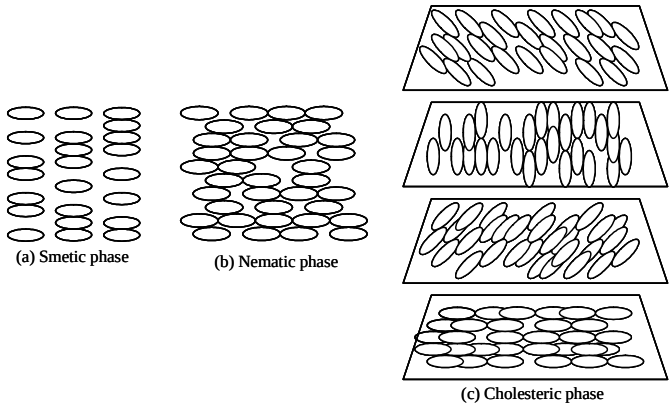

Fig. 1.2: Phases of liquid crystal (a) smetic phase; (b) nematic phase; (c) cholesteric phase.

1.2.2 Orientational Order Parameter

In the nematic phase, the molecules are rodlike with their long axes aligned barely parallel to one another. Thus at any point in the medium, we can define a vector $\widehat{n}$ to present the preferred orientation in the immediate neighborhood of the point. This vector is known as the director. In a homogeneous nematic LC, the director is a constant throught the medium. In an inhomogeneous nematic liquid crystal, the director $\widehat{n}$ can change form point to point and is, in general, a function of space (x, y, z). If we define a unit vector to represent the long axis of each molecule, then the director $\widehat{n}$ is the statistical average of the unit vectors over a small volume element around the point.

The order parameter S of a LC is defined as

$$S = \frac{1}{2}\left\langle 3\cos^2\theta - 1\right\rangle, \tag{1.1}$$

where θ is the angle between the long axis of an individual molecule and the director n and the angular brackets denote a statistical average. For perfectly parallel alignment, $S = 1$, while for totally random orientations, $S = 0$. In the nematic phase, the order parameter S has an intermediate value that is strongly temperature dependent. As the clearing point is approached, the order parameter S drops abruptly to zero. Typical values of the order parameter S are in the range between $0.4-0.6$ at low temperatures. The values of the order parameter S also depend on the structure of the molecules [22].

1.2.3 Refractive Index

In a glass container, nematic LCs often appear as an opaque milky fluid. The scattering of light is due to the random fluctuation of the refractive index of the sample. With no proper boundaries to define the preferred orientation, the sample consists of many domains of nematic LC. The discontinuity of the refractive index at the domain boundaries is the main cause of the scattering leading to the milky appearance. Under the proper treatment (rubbing the alignment layer on the glass substrate or chemical treatment), a slab of nematic LC can be obtained with an uniform alignment of the director. Such a sample exhibits uniaxial optical symmetry with two principal refractive indices n_o and n_e. The ordinary refractive index n_o is for light with electric field polarization perpendicular to the director and the extraordinary re-

fractive index n_e is for light with electric field polarization parallel to the director. The birefringence (optical anisotropy) is defined as

$$\Delta n = n_e - n_o. \tag{1.2}$$

If $n_o < n_e$, then the LC is said to be positive birefringent, whereas if $n_e < n_o$, then it is said to be negative birefringent. In classical dielectric theory, the macroscopic refractive index is related to the molecular polarizability at optical frequencies. The existence of the optical anisotropy is due mainly to the anisotropic molecular structures. Most LCs with rodlike molecules exhibit positive birefringence ranging from 0.05 to 0.7 [22].

1.3 Basic LCD components

The LCDs are composed by electrodes and a LC cell. To allow transmission of light, the electrodes must be transparent in the spectral regime of interest. This requires transparent materials with a good electrical conductivity. In LCD applications, ITO (indium tin oxide) is usually used because of its higher electrical conductivity. All transparent conductors exhibit a small absorption of light. As a result of the index mismatch between the glass substrate and the electrode materials, a Fabry-Perot cavity is formed in each of the electrodes which are sandwiched between glass and the LC as show the Fig. 1.3. A proper choice of the thickness ensures construc-

tive interference to maximize the transmission of light. In typical electrodes, the ITO thickness is in the range of $100 - 300nm$.

Typical thicknesses of the LC cell are in the range of a few μm. There are several LC configurations that can be employed for display applications. However, here only it will be described two configurations because those configurations are usually used in SLMs.

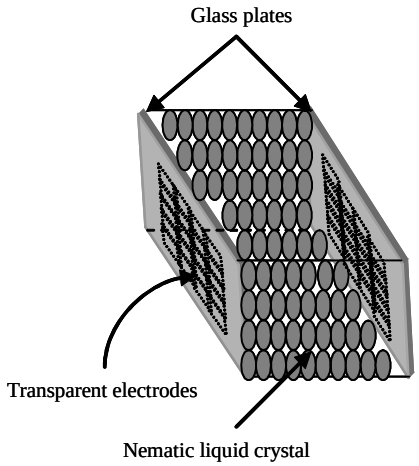

Figure 1.3. LCD components

1.4 Twisted nematic displays

In a twisted nematic (TN) display, each of the cells consists of a LC material sandwiched between two glass plates separated by a gap of 5-10 μm. The inner surfaces of the plates are deposited with transparent electrodes made of conductive coatings of ITO. These transparent electrodes are coated with a thin layer of polyimide

with a thickness of several hundred angstroms. The polyimide films are unidirectionally rubbed to ensure that the local directors are parallel to the rubbing directions at the surfaces. In a 90° TN, the rubbing direction of the lower substrate is perpendicular to the rubbing direction of the upper surface. Thus in the inactivated state (field off), the local director undergoes a continuous twist of 90° in the region between the plates as show the Fig. 1.4 [22].

If a beam of linearly polarized light propagates in a twisted nematic (TN) liquid crystal cell along the direction of the twist axis, then the polarization state of the light will follow the twist of the local director as the light propagates in the LC. This leads to a rotation of the output polarization state.

In the activated state (field on), a strong electric field built up in the liquid crystal. As a result of the dielectric anisotropy, the liquid crystal are aligned parallel to the direction of the applied electric field and therefore perpendicular to the substrate. The transmission of light through a TN liquid crystal depends of the orientation of the local $\widehat{n}$ axis (director) that is a function of position in the medium. As a result of the twisting of the $\widehat{n}$ axis, the medium is not homogeneous.

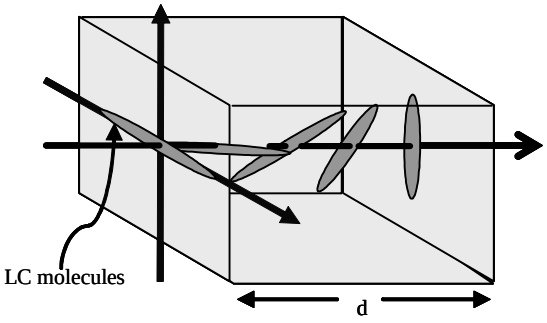

Figure 1.4. Twisted Nematic Liquid Crystal Display (field off).

Assuming that the twisting is linear and the azimuth angle of the axes is given by [22]

$$\psi(z) = \alpha z, \tag{1.3}$$

where z is the distance in the direction of propagation and α is a constant. If Γ is the phase retardation of the untwisted plate, in particular, for the case of nematic LC with $\widehat{n}$ parallel to the plate surfaces, then Γ is given by

$$\Gamma = \frac{2\pi}{\lambda}(n_e - n_o)d, \tag{1.4}$$

where d is the thickness of the plate, n_e, n_o are the principal refractive indices of the LC material. The total twist angle is

$$\phi \equiv \psi(d) = \alpha d. \tag{1.5}$$

The Jones matrix for TN display is given by [22]

$$\begin{pmatrix} \cos\sigma - i\frac{\Gamma \sin\sigma}{2\sigma} & \phi\frac{\sin\sigma}{\sigma} \\ -\phi\frac{\sin\sigma}{\sigma} & \cos\sigma + i\frac{\Gamma\sin\sigma}{2\sigma} \end{pmatrix}, \tag{1.6}$$

where

$$\sigma = \sqrt{\phi^2 + \left(\frac{\Gamma}{2}\right)^2}. \tag{1.7}$$

This Jones matrix changes its structure under the application of an external electric field because the n_e index depends of LC molecules tilt (θ) as shows the Fig. 1.5. The $n_e(\theta)$ index is given by

$$\frac{1}{n_e^2(\theta)} = \frac{\sin^2\theta}{n_o^2} + \frac{\cos^2\theta}{n_e^2}, \tag{1.8}$$

it is important to note that θ depends on the applied electric field.

To determine the amplitude and phase modulation provided by a TN SLM, it is placed between two polarizers as shows the Fig. 1.6. The incident polarized beam can be expressed by the Jones vector

$$J_i = \begin{pmatrix} \sin\varphi_1 \\ \cos\varphi_1 \end{pmatrix}, \tag{1.9}$$

where φ is the angle formed by the director axis of the polarizer, respect to the director axis of the LC molecules on the frontal face of the TN SLM. Then employing the matrix of the TN SLM given by the Eq. (1.6) and the matrix of the analizer, can be obtained the output polarized state given by

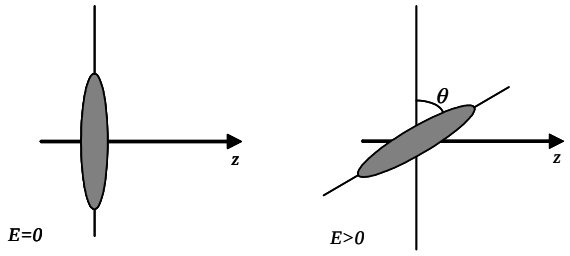

Fig. 1.5: LC molecules inclination due to an external electric field.

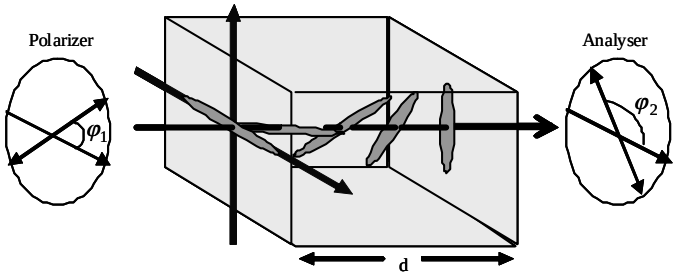

Figure 1.6. Arrangment to determine the modulation of a TN SLM.

$$J_{out} = \begin{pmatrix} \cos\varphi_2 & \sin\varphi_2\cos\varphi_2 \\ \sin\varphi_2\cos\varphi_2 & \sin\varphi_2 \end{pmatrix} \begin{pmatrix} \cos\sigma - i\frac{\Gamma\sin\sigma}{2\sigma} & \phi\frac{\sin\sigma}{\sigma} \\ -\phi\frac{\sin\sigma}{\sigma} & \cos\sigma + i\frac{\Gamma\sin\sigma}{2\sigma} \end{pmatrix} \begin{pmatrix} \sin\varphi_1 \\ \cos\varphi_1 \end{pmatrix}, \tag{1.10}$$

considering this output polarized beam is possible determine the amplitude and phase modulation.

In the practice the SLMs are controled with a computer. The electronic interface between the SLM and the computer provides the voltage that drives each pixel, the interface applies an electric filed whose value is represented as gray levels. In

general the TN SLMs modify the incident polarized beam by eliptic polarized states, so that the amplitude and phase modulations are coupled.

To determine the amplitude modulation are displayed gray levels (0-255) on the SLM, the amplitude modulation is proportional to the transmitted light through the analizer (Fig. 1.6).

For the case of the phase modulation, it can be determined measuring the zero order intensity of the diffraction pattern produced by a binary grating. The diffraction pattern produced by the binary grating consists of many orders as is shown in Fig. 1.7, but due to the zero order intensity contains the information of the phase modulation provided by the binary grating, only is necessary to consider this order. A plane wave illuminates the binary grating implemented on the SLM, which has two fringes of equal width, after the transmission the plane wave adquieres the phase modulation, $\exp(i0)$ and $\exp(i\phi_g)$ (where g adopts values from 0 to 255). The amplitude of the zero order, at the Fourier plane of the lens, is given by [23]

$$A_{0g} = 1 + \exp(i\phi_g), \tag{1.11}$$

therefore the power in the zero-th order diffracted, which is proportional to the square modulus of the amplitude, is given by

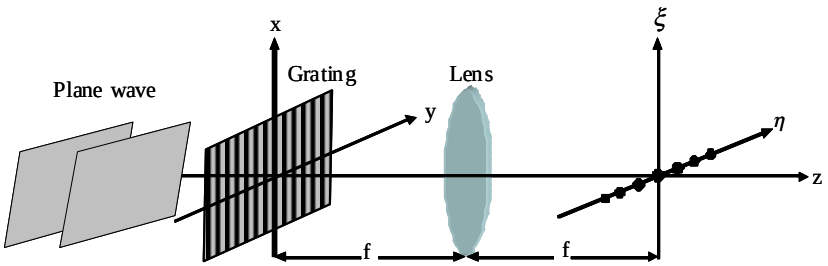

Figure 1.7: Diffaction pattern of a binary grating.

$$P_{0g} = |A_{0g}|^2 = 2 + 2\cos(\phi_g), \tag{1.12}$$

then the phase modulation (ϕ_g) can be found as a function of the gray level by

$$\cos(\phi_g) = \frac{P_{0g} - 2}{2}. \tag{1.13}$$

As an example the Fig. 1.8 shows the amplitude and phase modulation provided by a TN SLM with angles 25^o and 115^o of the polarizer and analyzer, respectively.

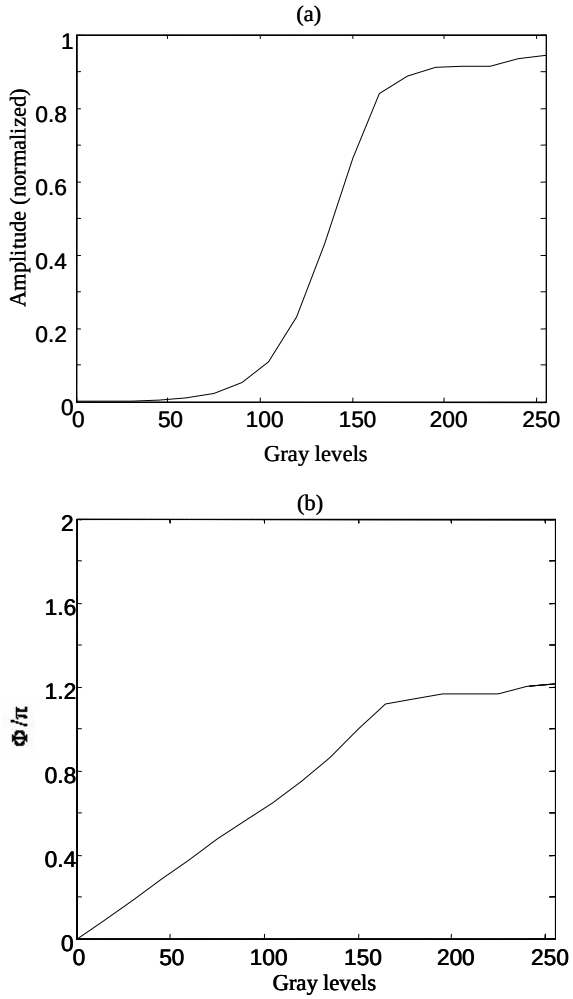

Figure 1.8. Modulation provided by a TN SLM at angles 25^o and 115^o of the polarizer and analyser, respectively, (a) amplitude modulation and (b) phase modulation

1.5 Parallel aligned LC cell displays

In a parallel aligned nematic liquid crystal display (N-LCD), the director axis of the LC molecules has the same orientation along the width of the LC cell (d), as

is shown in the Fig. 1.9. This type of alignment is regularly used in the phase-only SLMs because by illuminating it with a linearly polarized beam oriented parallel to the LC director axis, the polarization state of the incident beam does not change and the phase modulation is given by

$$\Gamma = \frac{2\pi}{\lambda} \int_0^d [n_e(\theta) - n_o]\, dz, \tag{1.14}$$

where $n_e(\theta)$ is given by Eq. (1.8), λ is the wavelength of the incident light.

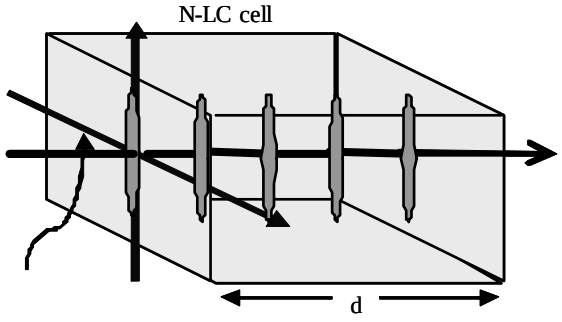

Figure 1.9. Nematic liquid Crystal display (N-LCD) using a parallel aligned cell.

Therefore to determine the phase modulation can be employed the method described in the previous section.

Chapter 2

Holography

2.1 Introduction.

Holography is a method that exploit interference, so it is not surprising to find a large number of applications of holography in interferometry. Holography allows the study of transparent objects, a capability not available to conventional interferometry. Holography also provides interferometry the capability of comparing a storage wavefront with a wave produced at a different location or at a different time.

A hologram is capable of producing a three-dimensional image of any object. The way to make a hologram is to divide a light wave into two mutually coherent waves. One wave, called the reference wave, illuminates the recording medium. The reference wave provides the bias needed for recording both the amplitude and phase of the signal wave. The second coherent wave illuminates the object of interest and the light scattered, from the object, creates the signal wave. The signal and the reference wave interfere at the hologram plane and a light-sensitive medium records the spatial intensity distribution of the interference. The recorded interference pat-

tern diffracts the reconstruction wave into an image wave. If one looks through the recording, called a transmission hologram, then one will see a three-dimensional image of the original object created by the image wave [24]

Below it will be described briefly, only as illustrative information, the basic theory of off-axis thin optical holograms whose concepts are the basis of the CGHs.

2.2 Thin optical holograms.

Any hologram in which the thickness of the recording material is small compared with the average spacing of the interference fringes can be classified as a thin hologram. Such a hologram can be characterized by a spatially varying complex trasmittance given by

$$t(x,y) = a(x,y)\exp\left[-i\phi(x,y)\right], \tag{2.1}$$

where $a(x,y)$ is the amplitude and $\phi\,(x,y)$ the phase.

2.2.1 The off-axis (Leith-Upatnieks) hologram

In the on-axis recorded holograms (Gabor), the image and noise were overlaped . Therefore the applications of these holograms were limited. The first successful technique for separating the image and noise was developed by Leith & Upatnieks

(1962). As it is shown in Fig. 2.1, a separate reference beam derived from the same coherent source is allowed to fall on the photographic plate at an offset angle θ to the optical axis. For simplicity, this reference beam can be assumed to be a plane wave. Assuming that the photographic plate is on the plane $z = 0$, only the variations over the plane (x, y) will be considered. Moreover, the temporal dependence of the waves $(e^{-i\omega t})$ will be omited, because the theoretical discussion only occur over the spatial coordinates.

The complex amplitude due to the object beam at any point (x, y) on the photographic plate can be written as

$$O(x, y) = O_0(x, y) \exp\left[-i\varphi(x, y)\right], \tag{2.2}$$

while the complex amplitude of the reference wave is

$$R(x, y) = R_0 \exp(i2\pi\xi_r x). \tag{2.3}$$

Since the reference wave has uniform intensity and only its phase varies across the photographic plate by the spatial frequency $\xi_r = \sin\theta/\lambda$. The resultant intensity distribution at the photographic plate due to the interference of the both beams is

$$I(x, y) = \left|R(x, y) + O(x, y)\right|^2 = R_0^2 + O_0(x, y)^2 + 2R_0 O_0(x, y) \cos\left[2\pi\xi_r x + \varphi(x, y)\right]. \tag{2.4}$$

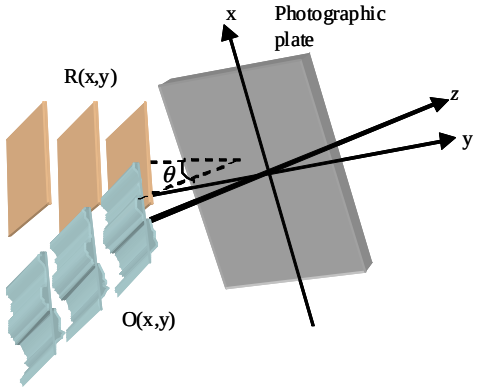

Figure 2.1. Hologram recording with an off-axis reference beam.

As can be seen from the third term on the right-hand side of Eq. (2.4) the amplitude and phase of the object wave, immerse on a background intensity noise given by the first and second terms on the right-hand of Eq. (2.4), are encoded as amplitude modulation, of a set of interference fringes, equivalent to a spatial carrier with a spatial frequency equal to ξ_r.

Assuming that the amplitude transmittance of the photographic plate after processing is linearly related to the intensity in the interference pattern, which is the most usual case, the amplitude transmittance of the hologram can be written as [25]

$$t(x,y) = t_0 + \gamma T \left\{ R_0^2 + O_0(x,y)^2 + R_0 O_0(x,y) \exp\left[-i\varphi(x,y)\right] \exp(-i2\pi\xi_r x) + R_0 O_0(x,y) \exp\left[i\varphi(x,y)\right] \exp(i2\pi\xi_r x) \right\}; \quad (2.5)$$

where γ is the slope of the amplitude transmittance versus exposure characteristic of the photographic material, T is the exposure time and t_0 is a constant background

transmittance. To reconstruct the image, the hologram is illuminated once again, as shows the Fig. 2.2, with the same reference wave. The complex amplitude $u(x, y)$, which is valid only on a small distance z behind the hologram, of the transmitted reference beam is the sum of four terms, each corresponding to one of the terms of Eq (2.5), and can be written as

$$u(x, y) = R(x, y)t(x, y) = u_1(x, y) + u_2(x, y) + u_3(x, y) + u_4(x, y), \tag{2.6}$$

where

$$u_1(x, y) = t_0 R_0 \exp(i2\pi\xi_r x), \tag{2.7}$$

$$u_2(x, y) = \gamma T R_0 O_0(x, y)^2 \exp(i2\pi\xi_r x), \tag{2.8}$$

$$u_3(x, y) = \gamma T R_0^2 O(x, y), \tag{2.9}$$

$$u_4(x, y) = \gamma T R_0^2 O^*(x, y) \exp(i4\pi\xi_r x), \tag{2.10}$$

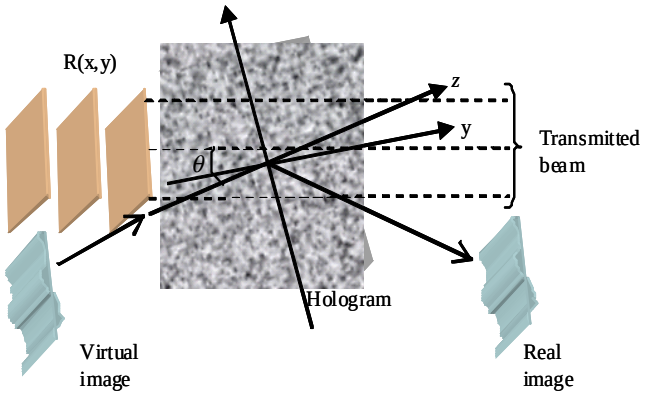

Figure 2.2. Image reconstruction by a hologram recorded with an off-axis reference beam.

The first term on the right hand side of Eq. (2.6), $u_1(x, y)$, is merely the attenuated reference beam, which is a plane wave directly transmitted through the hologram. This directly transmitted beam is surrounded by a spatially varying halo due to the second term, $u_2(x, y)$. The angular spread of this halo is determined by the angular extent of the object.

The third term, $u_3(x, y)$ is identical to the original object wave, except for a constant factor, and generates a virtual image of the object in its original position; this wave makes an angle θ with the directly transmitted wave. Similarly, the fourth term, $u_4(x, y)$, gives rise to the conjugate real image. However, in this case, the fourth term includes an exponential factor, $\exp(i4\pi\xi_r x)$, which indicates that the conjugate wave is deflected off the axis at an angle approximately twice of the reference wave.

Thus, two images angularly separated, one real and one virtual, are reconstructed in this setup, from the directly transmitted beam. If the offset angle θ of the reference beam is made large enough, then it is possible to ensure that there is no overlap between the halo and the image. This method therefore eliminates all the major drawbacks of Gabor's original in-line arrangement. The spatial carrier frequency (ξ_r) determines the offset angle θ required to ensure that each of the images can be observed without any interference from its conjugated

The angular spectra of the Fourier transforms of the attenuated reference beam and its halo, Eqs. (2.7) and (2.8), are given by

$$U_1(\xi,\eta) = f\left\{t_0 R \exp(i2\pi\xi_r x)\right\} = t_0 R\delta(\xi+\xi_r,\eta), \tag{2.11}$$

$$\begin{aligned} U_2(\xi,\eta) &= f\left\{\gamma TR\left|O(x,y)\right|^2 \exp(i2\pi\xi_r x)\right\} \\ &\quad \gamma TR\left[O(\xi,\eta)\otimes O(\xi,\eta) * \delta(\xi+\xi_r,\eta)\right], \end{aligned} \tag{2.12}$$

where the symbols $\otimes$ and $*$ denote the operations of correlation and convolution, respectively. Meanwhile the Fourier transform of the real object and its conjugate are

$$U_3(\xi,\eta) = f\left\{\gamma TR^2 O(x,y)\right\} = \gamma TR^2 O(\xi,\eta), \tag{2.13}$$

$$\begin{aligned} U_4(\xi,\eta) &= f\left\{\gamma TR^2 O * (x,y)\exp(i4\pi\xi_r x)\right\} = \\ &\quad \gamma TR^2 O * (\xi,\eta) * \delta(\xi+2\xi_r,\eta), \end{aligned} \tag{2.14}$$

respectively. As can be seen from Fig. 2.3, that schematically shows these spectra , the term $|U_3(\xi,\eta)|$ is merely the object-beam spectrum multiplied by a constant and is centred at the origin of the spatial frequency plane. The term $|U_1(\xi,\eta)|$ corresponds to the spatial frequency of the carrier fringes and is a delta function located at $(-\xi_r,0)$, while $|U_2(\xi,\eta)|$ is centred on this delta function and, it is proportional to the auto-correlation function of $O(\xi,\eta)$, has twice the extent of the object-beam spectrum. Finally, $|U_4(\xi,\eta)|$ is similar to $|U_3(\xi,\eta)|$ but displaced to a centre frequency $(-2\xi_r,0)$.

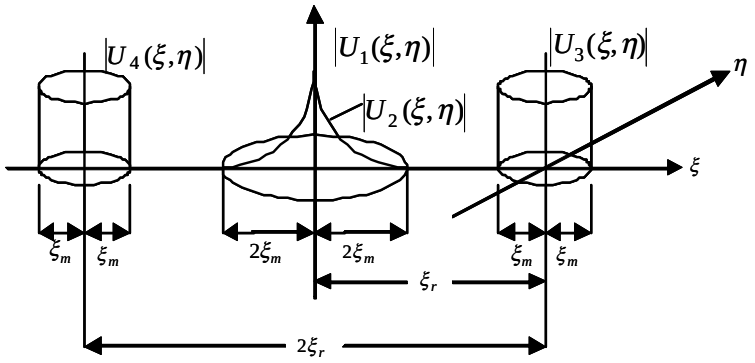

Figure 2.3. Spatial frequency spectra of a hologram recorded with an off-axis reference beam.

Evidently, $|U_3(\xi,\eta)|$ and $|U_4(\xi,\eta)|$ will not overlap. $|U_1(\xi,\eta)|$ and $|U_2(\xi,\eta)|$ if the spatial carrier frequency ξ is chosen so that

$$\xi_r \geq 3\xi_m, \tag{2.15}$$

where ξ_m is the largest spatial frequency component of the object [25].

2.2.2 Thin phase holograms

In a similar way to the off-axis amplitude holograms, there are holograms that can be formed on recording media in which $t(x,y)$ is a complex function, that is, the hologram alters only the phase of the illuminating wave in correspondence with the recording exposure. Such hologram is called a "phase hologram" and has some interesting and important properties.

Assuming that a recording medium is such that a phase modulation $\psi(x,y)$ results in a change in index $n(x,y)$ of the medium, the exposed hologram will have

a phase variation of the form $khn(x,y)$. This imposed phase modulation yields various diffracted orders, the $\pm 1^{st}$ orders producing the desired reconstructions, as it will be discussed below.

Exposing a recording medium to an object wave described by

$$O(x,y) = O_0(x,y)e^{i\varphi(x,y)}, \tag{2.16}$$

and a plane reference wave

$$R(x,y) = R_0 e^{i\beta x}; \tag{2.17}$$

where $\beta = k\sin\alpha_R$, k is the wave number, as shows the Fig 2.4. Considering that the final phase modulation to be imposed, on the illuminating wave, is determined by the intensity distribution given by

$$I(x,y) = |O(x,y) + R(x,y)|^2 = O_0(x,y)^2 + R_0^2 + 2O_0(x,y)R_0\cos(\varphi(x,y) - \beta x), \tag{2.18}$$

the complex transmittance function then becomes [25]

$$t(x,y) = t_0 e^{iI(x,y)} = B(x,y)e^{ia(x,y)\cos(\theta(x,y))}, \tag{2.19}$$

where

$$\begin{aligned} B(x,y) &\equiv t_0 e^{iO_0(x,y)^2} e^{iR_0^2}, \\ a(x,y) &\equiv 2O_0(x,y)R_0, \\ \theta(x,y) &\equiv \varphi(x,y) - \beta x. \end{aligned} \tag{2.20}$$

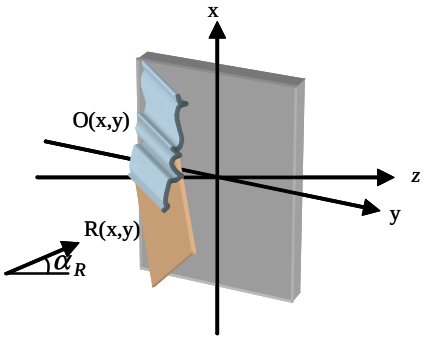

Figure 2.4. Recording a hologram

The complex transmittance can be expressed, employing the Jacobi-Anger identity [26], by

$$t(x,y) = B(x,y)\left\{\begin{array}{l} J_0(a(x,y)) + 2\sum_{n=1}^{\infty}(-1)^n J_{2n}(a(x,y))\cos(2n\theta(x,y)) \\ +2i\sum_{n=0}^{\infty}(-1)^{n+2} J_{2n+1}(a(x,y))\cos[(2n+1)\theta(x,y)] \end{array}\right\}, \tag{2.21}$$

where $J_n(a(x,y))$ are the Bessel functions of the first kind. Each $J_n(a(x,y))$ function represents the amplitude of the nth diffracted order.

The term of Eq(2.21) leading to the images of interest, which to contain the phase of the object wave, is the term with $n = 0$ and is given by

$$B(x,y)\left[2iJ_1(a(x,y))\cos\left[\theta(x,y)\right]\right], \tag{2.22}$$

which can be written as

$$2iB(x,y)J_1(a(x,y))\left(\frac{e^{i\theta(x,y)} + e^{-i\theta(x,y)}}{2}\right) = iB(x,y)J_1(a(x,y)) \tag{2.23}$$
$$\left(e^{i(\varphi(x,y)-\beta x)} + e^{-i(\varphi(x,y)-\beta x))}\right),$$

the two terms in Eq. (2.23) represent the primary and conjugate image waves. The transmission term leading to the primary image is

$$t_p(x,y) = t_0 \exp\left[i\left(O_0(x,y)^2 + R_0^2 + \frac{\pi}{2}\right)\right] J_1(2O_0(x,y)R_0)e^{i(\varphi(x,y)-\beta x)}. \quad (2.24)$$

If the hologram is illuminated with the reference wave $R(x,y)$, as is shown in Fig. 2.5, then the primary image wave is

$$\psi_p(x,y) = R(x,y)t_p(x,y) = t_0 e^{i\left(O_0(x,y)^2+R_0^2+\pi/2\right)} R_0 J_1(2O_0(x,y)R_0)e^{i\varphi(x,y)}. \quad (2.25)$$

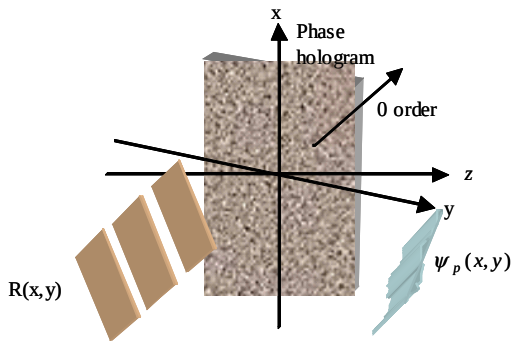

Figure 2.5. Diffraction from a phase hologram.

If the product $2O_0(x,y)R_0$ is small, then $\psi_p(x,y)$ can be expressed as

$$\psi_p(x,y) \cong \frac{t_0}{2} e^{i\left(O_0(x,y)^2+R_0^2+\pi/2\right)} R_0^2 O_0(x,y)e^{i\varphi(x,y)}; \quad (2.26)$$

which is seen to be, aside from the unimportant phase and amplitude factors, just the original object wave. If the product $2O_0(x,y)R_0$ is large, then some amplitude distortions will be present.

As it was discussed above, to record an optical hologram, it was necessary to have physically the object to codify. Nevertheless, for some applications it is more addecuated only to have a digital representation of the object. Therefore in 1966 A. W. Lohmann and his collegues invented the computer generated holograms (CGHs), these allow to create a hologram only defining mathematically the wavefront to codify. Moreover the CGHs have the remarkable advantage, over the optical holograms, that their perfomance can be evaluated numerically. Therefore the use of CGHs have increased enormously. In the next section the CGHs will be discussed.

2.3 Computer-generated holograms

Computer generated holograms allow the generation of wavefronts with any desired amplitude and phase distribution. The production of holograms using a digital computer has been reviewed in detail by Lee [27], Yaroslavski & Merzlyakov [28] and Dallas [29].

The purpouse of CGHs is to codify the complex amplitude of an object wave at the hologram plane; for convenience this is usually taken to be the Fourier transform of the complex amplitude in the object plane. It can be shown, by means of the sampling theorem, that if the object wave is sampled at a sufficiently large number of points, then no loss of information is obtained. Thus, for an image consisting of $N \times N$ resolvable elements to be reconstructed, the object wave is sampled at $N \times N$

equally spaced points, and the $N \times N$ complex coefficients of its discrete Fourier transform can be evaluated. This can be done quite easily with a computer program using the fast Fourier transform algorithm [30].

The recording and reconstruction of the first CGH was cumbersome. In this case, the computer is used to control a plotter which produces a large-scale version of the hologram. Then, it is photographically reduced and bleached to produce the required transparency. However this approach is complex, expensive and does not work in real time.

In recent years the use of SLMs have revolutionated the field of CGHs because their electrically addressability feature can provide precise, repeatable, and reconfigurable optical modulation patterns. In this sense, the SLMs have become a very useful tool for CGH applications. Due to the SLMs can modulate amplitude or phase of the light, with these can be implemented amplitude holograms and phase holograms. The amplitude CGHs, implemented on SLMs, present good quality in the generation of complex fields [31], however their intensity efficiency is very low. The phase CGHs, implemented on SLMs, have had a major development because these present a good quality in the generation of complex fields, and the intensity efficiency is higher than the amplitude CGHs. Therefore in the most of applications the phase CGHs are employed.

In the next sections are presented two novel types of phase CGHs called synthetic phase holograms (SPHs), which are one of the contributions reported in this thesis.

2.4 Synthetic phase holograms.

The purpose is to generate an arbitrary complex optical field, whose amplitude and phase modulation are independently specified. This complex field can be expressed as

$$s(x,y) = a(x,y)\exp[i\phi(x,y)], \tag{2.27}$$

where $a(x,y)$ and $\phi(x,y)$ denote respectively the amplitude and the phase of the field. These functions can take values in the real intervals [0,1] and [-π,π] respectively. Thus, the possible values of the function $s(x,y)$ belong to the circle of unitary radius, which is denoted as Ω_S, centered at the origin of the complex plane. The aim is to encode the complex field $s(x,y)$ into a phase transmittance hologram. A general hologram that encode the arbitrary complex modulation $s(x,y)$ is a constrained complex transmittance, whose possible values belong to a subset of the unitary circle Ω_S. In the particular case of phase holograms, this subset is formed by the complex points of unitary modulus. For simplicity, the explicit dependence of the amplitude $a(x,y)$ and the phase $\phi(x,y)$ on the spatial coordinates (x,y), in the next discussion,

will be omited. The general transmittance of a synthetic phase hologram (SPH), expressed as a function explicitly dependent on the amplitude and the phase of the field to be encoded , is given by

$$h(x,y) = \exp\left[i\psi(a,\phi)\right], \tag{2.28}$$

where $\psi(a,\phi)$ is the hologram phase modulation. The aim is to establish phase functions with the form of Eq. (2.28) that provide the appropriate encoding of the complex field $s(x,y)$. A fruitful method to determine appropriate forms of the hologram phase $\psi(\phi,a)$ is based on the representation of $h(x,y)$ by a Fourier series expansion in the domain of ϕ. According to this Fourier series the SPH transmittance can be expressed as

$$h(x,y) = \sum_{q=-\infty}^{\infty} c_q^a \exp(iq\phi), \tag{2.29}$$

$$c_q^a = (2\pi)^{-1} \int_{-\pi}^{\pi} \exp[i\psi(\phi,a)] \exp(-iq\phi) d\phi. \tag{2.30}$$

In Eq. (2.30) it is noted that after integration in the variable ϕ, the resulting coefficients c_q^a are explicitly dependent on the amplitude a. From Eq. (2.29) is easy to see that the term $q = 1$ gives the phase ϕ of the $s(x,y)$ function. Therefore the appropriate condition for signal encoding in the SPH is given by

$$c_1^a = Aa, \tag{2.31}$$

for a positive constant A. If the signal encoding condition is fulfilled, then the first order term in the hologram Fourier series, $s_1(x,y)$, corresponds to the encoded field

$s(x, y)$ (except by a positive factor A). As the exponential term in Eq. (2.30) can be divided in real, and imaginary parts, the sufficient and necessary conditions to fulfill Eq. (2.31) are given by the following identities

$$\int_{-\pi}^{\pi} \sin[\psi(\phi, a) - \phi] d\phi = 0, \tag{2.32}$$

$$\int_{-\pi}^{\pi} \cos[\psi(\phi, a) - \phi] d\phi = 2\pi A a. \tag{2.33}$$

Equations (2.32) and (2.33) represent a useful basis for determination of appropriate SPHs. It is noted that the maximum value of the integral in Eq. (2.33) is 2π. In consequence the maximum possible value of constant A (for appropriate encoding) is equal to unity. Although it is possible to find a great variety of solutions of Eqs. (2.32) and (2.33), now the attention is focused on functions $\psi(\phi, a)$ with odd symmetry in the variable ϕ. It is not difficult to show that the symmetry of such functions ensures the fulfillment of Eq. (2.32).

2.4.1 Modification of the SPH by a phase carrier

The reconstruction of the encoded field is performed by spatial filtering in the hologram's Fourier spectrum plane. The Fourier spectrum of the field $s(x, y)$ is denoted by $S(u, v)$, where (u, v) represent the spatial frequency coordinates associated to the spatial coordinates (x, y). It is assumed that the Fourier spectrum $S(u, v)$ is centered on the spatial frequencies $(u, v) = (0, 0)$, in the hologram's Fourier plane.

Thus, the spectra for the different terms in the hologram Fourier expansion [in Eq. (2.29)] are also centered at the Fourier plane axis. In consequence, the encoded field can not be recovered by spatial filtering, from the PSH defined in Eq. (2.28). In order to achieve the spatial isolation of the encoded field, the above definition of the PSH is modified by adding the linear phase modulation to the phase of the encoded field. The linear phase modulation is

$$2\pi(u_0 x + v_0 y), \tag{2.34}$$

with (u_0, v_0) as the carrier spatial frequencies. Therefore the modified SPH transmittance, given by

$$h_c(x, y) = \exp[i\psi(\phi + 2\pi(u_0 x + v_0 y), a)], \tag{2.35}$$

can be expressed by the Fourier series [18]

$$h_c(x, y) = \sum_{q=-\infty}^{\infty} s_q(x, y) \exp\left[i2\pi(qu_0 x + qv_0 y)\right], \tag{2.36}$$

where $s_q(x, y) = c_q^a \exp(iq\phi)$. The Fourier spectrum of this modified SPH is given by

$$H_c(u, v) = \sum_{q=-\infty}^{\infty} S_q(u - qu_0, v - qv_0), \tag{2.37}$$

where $S_q(u, v)$ is the Fourier transform of $s_q(x, y)$. The structure of the SPH Fourier transform, formed by laterally shifted copies of the Fourier spectra $S_q(u, v)$, allows the spatial isolation of the encoded field. The recovered encoded field,

$$A\, s(x, y) \exp\left[i2\pi(u_0 x + v_0 y)\right], \tag{2.38}$$

obtained by spatial filtering, is only affected by the carrier phase tilt.

The Fourier spectrum in Eq. (2.37) corresponds to a SPH implemented with a phase modulator free of spatial quantization. Accurate implementation of SPHs without spatial quantization allows an efficient isolation of the encoded field from non-signal diffraction orders of the SPH, enabling reconstruction with high signal to noise ratio (SNR) given by [31]

$$SNR = \frac{\iint_{Ds} |s(x,y)|^2 \, dxdy}{\iint_{Ds} |s(x,y) - \beta s_t(x,y)|^2 \, dxdy}, \tag{2.39}$$

where $s(x,y)$ and $s_t(x,y)$ denote the ideal signal and the signal under evaluation, respectively,D_S is the domain where evaluation is performed, and the constant β is

$$\beta = \frac{\iint_{Ds} \mathrm{Re}\left\{s(x,y)s_t^*(x,y)\right\} dxdy}{\iint_{Ds} |s_t(x,y)|^2 \, dxdy}. \tag{2.40}$$

The unique restriction (common to all the SPH types) to obtain an acceptable SNR, is that at least one of the hologram carrier frequencies (u_0, v_0) must be larger than the bandwidth of the encoded field $s(x,y)$.

2.4.2 Implementation of SPH with a low resolution pixelated SLM.

If a SPH is implemented with a low resolution pixelated SLM, then the reconstructed signal term can be affected by high order diffraction contributions. In general, the noise level in the reconstructed field, introduced by the high order dif-

fraction terms is highly dependent on the SPH type. In the next section is proved that two proposed SPHs can generate the encoded complex field with remarkably high SNR, even if they are implemented on a pixelated SLM.

If the phase SLM employed to implement the SPHs has square pixels of dimensions b, and pixel pitch δx, then the Fourier spectrum of the pixelated SPH $h(x, y)$ is given by

$$H_{pix}(u, v) = E(u, v) \sum_{n=-\infty}^{\infty} \sum_{m=-\infty}^{\infty} H_c(u - n\Delta u, v - m\Delta u), \tag{2.41}$$

where $\Delta u = 1/\delta x$ is the SLM bandwidth, the factor $E(u, v)$, given by the Fourier transform of the pixel window, is

$$E(u, v) = b^2 \text{sinc}(bu)\text{sinc}(bv), \tag{2.42}$$

where $\text{sinc}(\alpha) = \sin(\pi\alpha)/\pi\alpha$.$H_c(u, v)$ is the Fourier spectrum of the continuous SPH given by Eq. (2.37). According to Eq. (2.41), the Fourier spectrum of the pixelated SPH is formed by the superposition of laterally shifted replicas of the spectrum $H_c(u, v)$ modulated by the pixel Fourier transform $E(u, v)$. The spectrum function $H_1(u - u_0, v - v_0)$ that appears at the term $H_c(u, v)$ of the series in Eq. (2.41) is equivalent to the signal spectrum $S(u - u_0, v - v_0)$. The distortion of the signal spectrum due to the factor $E(u, v)$ can be avoided by an appropriate prefiltering of the encoded field [31]. This process consists in replacing the original encoded field $s(x, y)$ by a modified field $s'(x, y)$ that is defined by its Fourier transform $S'(u, v)$

obtained from the relation $S'(u-u_0, v-v_0) = S(u-u_0, v-v_0)E^{-1}(u,v)$. The function $E^{-1}(u,v)$ is appropriately defined in the domain of $S(u-u_0, v-v_0)$ since the carrier frequencies(u_0, v_0) are always chosen in such a way that $S(u-u_0, v-v_0)$ is enveloped by a nonzero sector of $E(u,v)$.

An inconvenient consequence of the pixelated structure of the SPH is that the domain of the signal spectrum term $H_1(u-u_0, v-v_0)$ that is centered at the spatial frequency coordinates (u_0, v_0) may also contain high-order spectrum contributionsH_q from spectrum replicas $H_c(u-n\Delta u, v-m\Delta u)$. To analize the relative significance of the high-order spectrum terms H_q sharing the signal spectrum region, it is assumed that the carrier spatial frequencies are $u_0 = v_0 = (P/Q)\Delta u$ with relative prime integers P and Q (with $P/Q \leq \frac{1}{2}$). In this case, it is not difficult to prove that the spectra contributions that appear centered at the signal spatial frequencies (u_0, v_0) are $H_{QR+1}(u-u_0, v-v_0)$ for any arbitrary integer number R. The signal term in this set of spectra contributions correspond to $R = 0$.

To obtain a high SNR, the high-order contributions $H_{QR+1}(u-u_0, v-v_0)$ (with $R \neq 0$) must be negligible compared with the signal spectrum $H_1(u-u_0, v-v_0)$. Considering Eq. (2.41), it is clear that the power of the spectrum term $H_{QR+1}(u,v)$ is proportional to the squared modulus of the coefficient c^a_{QR+1}. The coefficients c^a_q for the SPHs of type 1 and 2 defined in Eqs. (2.47) and (2.50) in terms of Bessel

functions tend rapidly to zero when $|q|$ is increased. Thus, it is expected that these SPHs will enable reconstruction of the encoded field with relatively high SNR.

The significance of noise contribution $H_{QR+1}(u-u_0, v-v_0)$ in relation to the signal term $H_1(u-u_0, v-v_0)$ can be measured by the ratio

$$\rho = \frac{\left|c^a_{QR+1}\right|^2}{\left|c^a_1\right|^2}. \tag{2.43}$$

The parameter ρ is useful to evaluate the quality of SPHs without requiring knowledge of the encoded complex function $s(x, y)$. Lower values of ρ correspond to SPHs with higher immunity to the high-order noise terms that are transmitted in the SPH plane. The SNR provides another measure of the PSH performance. In the next section two novel types of SPHs will be discussed.

2.5 Generation of synthetic phase holograms

In this section the experimental generation of two novel SPHs is shown. The experimental setup is shown in Fig. 2.6. A He-Ne laser was expanded and collimated to illuminate completely the SLM active area where the SPH is displayed. The lens 1 takes the Fourier spectrum of the SPH, at the Fourier plane a filtering mask is placed to block the unwanted orders, and the lens 2 recovers the complex field to be captured with the CCD. As an example we chose to codify the nondiffracting Bessel beams and the Laguerre-Gauss beams because these fields are commonly studied in optics.

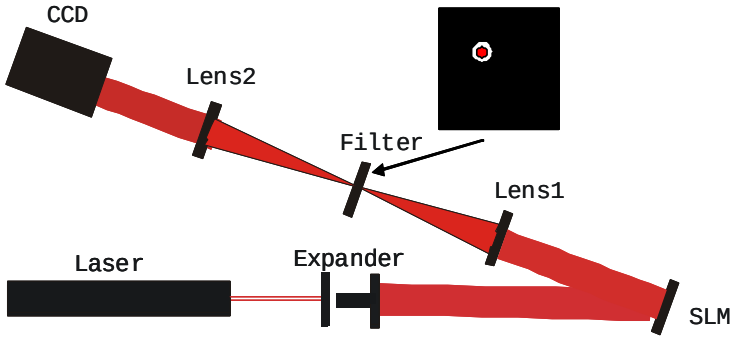

Figure 2.6. Experimental setup to generate the PSHs type 1 and type 2.

The Bessel beams in polar coordinates (r, θ) are given by

$$s_1(r, \theta) = J_n(2\pi r / r_0) \exp(in\theta), \tag{2.44}$$

where r_0 is the asymptotic radial period of the Bessel function J_n, and the Laguerre-Gauss Beams are expressed by

$$s_2(r, \theta) = \left(2r^2 / w_0^2\right)^{|l|/2} L_p^{|l|}\left(2r^2 / w_0^2\right) \exp\left(-r^2 / w_0^2\right) \exp(il\theta), \tag{2.45}$$

where $L_p^{|l|}$ denotes an associated Laguerre Polynomial, w_0 is the beam waist radius, p is the radial mode index, l is the phase singularity charge.

2.5.1 Synthetic phase hologram type 1

According to the theoretical discussion shown in section 2.4, a hologram phase modulation $\psi(\phi, a)$, with odd symmetry in ϕ, is given by [33]

$$\psi(\phi, a) = \phi + f(a) \sin(\phi). \tag{2.46}$$

In this case the SPH type 1 coefficients, according to Eq. (2.30) , are expressed in terms of the integer order Bessel functions J_n by [26]

$$c_q^a = J_{q-1}[f(a)]. \tag{2.47}$$

The encoding condition is valid (with $A = 1$) if $f(a)$ is obtained from the relation

$$J_0[f(a)] = a, \tag{2.48}$$

Eq. (2.48) can be fulfilled for every value of a in [0,1], taking the appropriate value of $f(a)$ in the domain [0,x_0] where $x_0 \cong 2.4048$ is the first root of the Bessel function $J_0(x)$. The resulting function $f(a)$, inverted numerically from Eq. (2.48), is shown in Fig. 2.7.

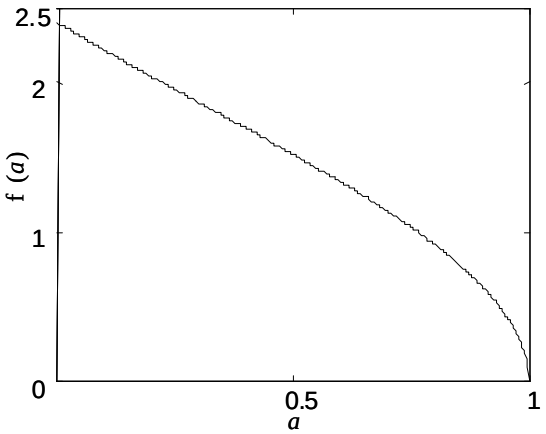

Figure 2.7. Function $f(a)$ versus a for the SPH of type 1.

For the generation of SPHs type 1 an only-phase reflection modulator (Boulder nonlinear system, Fig. 2.8) was employed, which has 512 x 512 pixels with a pixel pitch of δx =15 μm. The phase response to $\lambda = 0.6328\ \mu m$ is shown in the Fig. 2.9,

this phase response was obtained with the method described in the section 1.4. As shows the Fig. 2.9 the 2π phase modulation is achieved with 70 gray levels.

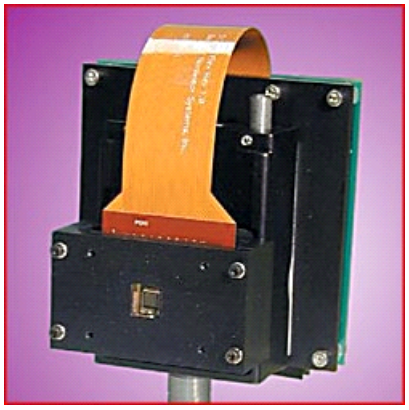

Figure 2.8. Reflective SLM with 512 x 512 pixels, Boulder Non Linear System.

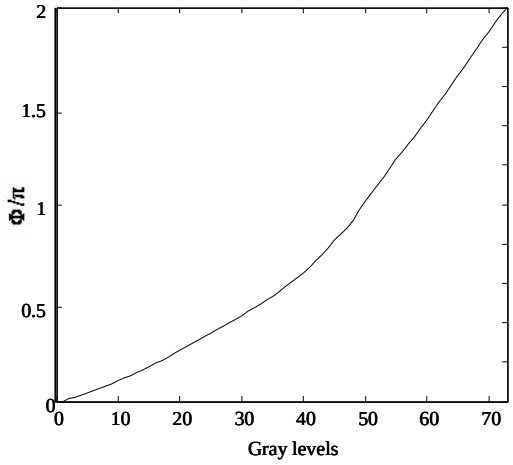

Figure 2.9. Phase modulation vs Gray levels to He-Ne laser

For all the encoded beams a finite circular support with a radius R equal to 100 pixels was employed, this type of support was chosen because its spectral distribution

helps to zero order noise affects less to the signal term. Both the radial period r_0 (for the Bessel beams) and the waist w_0 (for Laguerre-Gauss beams) were adopted as $R/4$. For isolation of the signal high-order diffraction terms, the carrier spatial frequency employed was $u_0 = v_0 = \Delta u/6$.A circular pupil in the Fourier domain of the PSHs employed as spatial filter for signal isolation was adjusted to optimize the quality of the generated fields. The application of this pupil to the signal spectrum represents a low-pass filtering during reconstruction of the encoded field. To increase the fidelity of the reconstrunted field it is necessary to increase the pupil diameter. However, if the diameter is too large, higher amounts of noise contribution will be transmitted by the pupil. Thus, in practice it is necessary to optimize this diameter for each particular SPH. The intensity distributions of the experimentally generated beams were recorded with a CCD camera. Intensity and CGH for the Bessel beam of order $n = 1$ is shown in Fig 2.10, the SNR for this beam is 2.04×10^3. This high SNR means that the reconstructed field has a good quality.

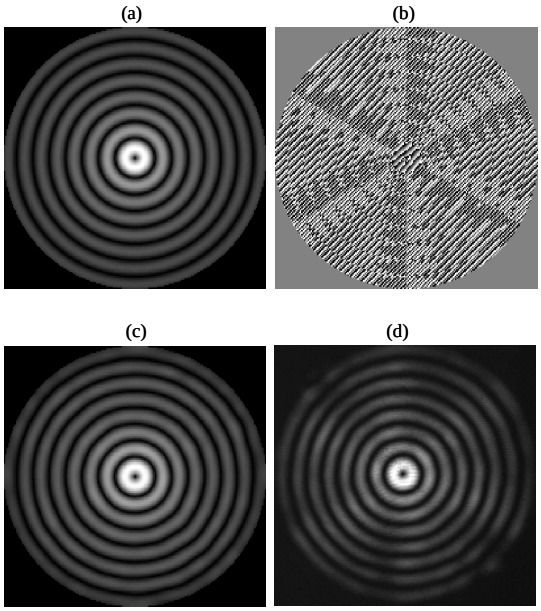

Figure 2.10. Bessel function generated with a support radius R = 100 pixels, r_0 = R/4, and a carrier spatiel frecuency $u_0 = v_0 = \Delta u/6$, n = 1, (a) Source function, (b) Hologram, (c) Theoretical reconstruction, with a SNR = 2.04×10^3, and (d) Experimental reconstruction.

The figure 2.11 shows the intensity and CGH for the Bessel beam of order $n = 3$, the SNR for this beam is 2.45×10^3.

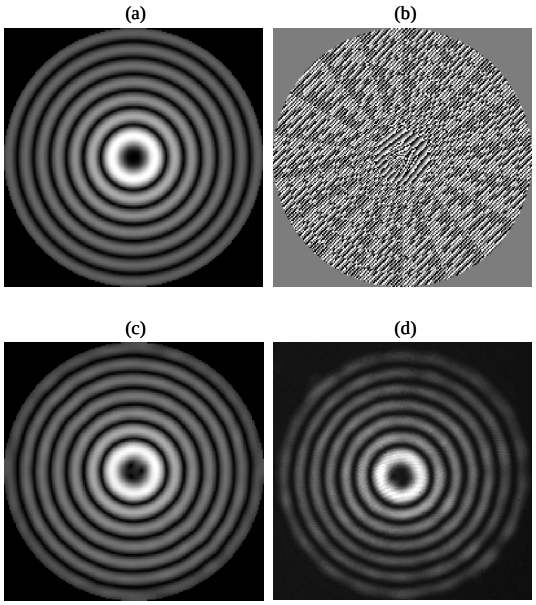

Figure 2.11. Bessel function generated with a support radius R = 100 pixels, r_0 = R/4, and a carrier spatiel frecuency $u_0 = v_0 = \Delta u/6$, n = 3, (a) Source function, (b) Hologram, (c) Theoretical reconstruction, with a SNR = 2.45×10^3, and (d) Experimental reconstruction.

The images of the generated Laguerre-Gauss beams with indices ($p.l$) of (0,2) and (2,4) are shown in Figs. 2.12 and 2.13, respectively.

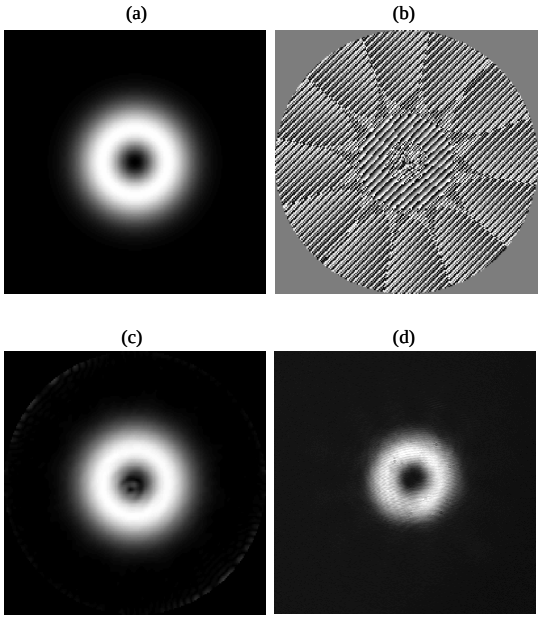

Figure 2.12. Laguerre-Gauss function generated with a support radius R = 100 pixels, r_0 = R/4, and a carrier spatiel frecuency $u_0 = v_0 = \Delta u/6$, (p,l) = (0,2), (a) Source function, (b) Hologram, (c) Theoretical reconstruction, with a SNR = 6.56×10^5, and (d) Experimental reconstruction.

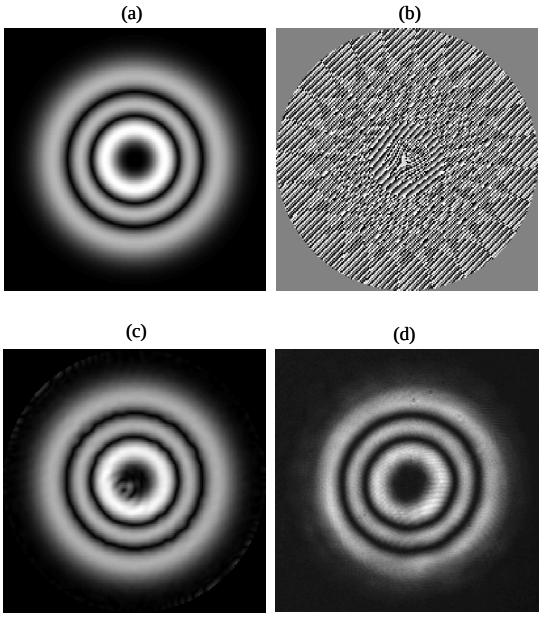

Figure 2.13. Laguerre-Gauss function generated with a support radius R = 100 pixels, r_0= R/4, and a carrier spatiel frecuency $u_0 = v_0 = \Delta u/6$, (p,l) = (2,4), (a) Source function, (b) Hologram, (c) Theoretical reconstruction, with a SNR = 3.17×10^5, and (d) Experimental reconstruction.

2.5.2 Synthetic phase hologram type 2

For this type of SPH, the hologram phase modulation is given by [33]

$$\psi(\phi, a) = f(a)\sin(\phi). \tag{2.49}$$

In this case the coefficients in the SPH Fourier series, according to Eq. (2.30), are given by [26]

$$c_q^a = J_q[f(a)], \tag{2.50}$$

and the encoding condition is fulfilled if $f(a)$ is inverted from the relation

$$J_1[f(a)] = Aa. \tag{2.51}$$

The maximum value of A for which Eq. (2.51) can be fulfilled is $A \cong 0.5819$, equal to the maximum value of the first order Bessel function $J_1(x)$, which occurs at $x = x_1 \cong 1.84$. The inverted function $f(a)$, which adopts values in the interval $[0, x_1]$, is depicted in Fig. 2.14. It is interesting to note that this SPH can be implemented with phase modulation in a reduced domain $[-f_0\pi, f_0\pi]$, with $f_0 \cong 0.586$. The total phase depth of the required modulator in this case is

$$\Delta\phi \cong 1.17\pi. \tag{2.52}$$

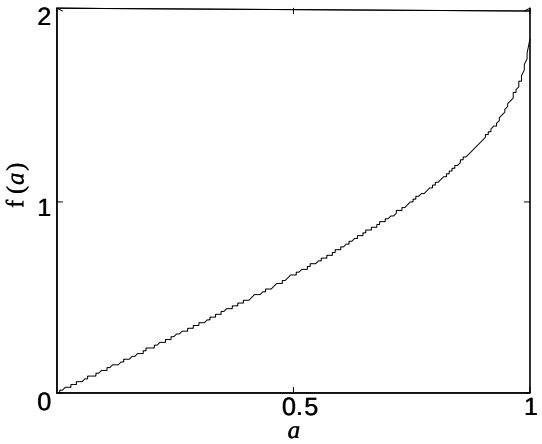

Figure 2.14. Function $f(a)$ versus a for the SPH of type 2.

A further reduction in this phase depth can be attained by adopting a smaller value of A in Eq. (2.51). An advantage of this reduced phase domain is that it can be obtained with conventional phase liquid crystal SLMs, employing relatively large wavelengths, e.g. in the near infrared spectrum region. The only undesirable effect is that the SPH efficiency is also reduced (by the factor A^2).

Due to that this type of SPH can be implemented with a reduced phase modulation, the device employed was a twisted nematic LC (LC2002 transmission SLM of Holoeye Photonics AG), with 600 x 800 pixels with a pixel pitch of $33\ \mu m$, shown in Fig. 2.15. This SLM was employed to show that, to codify the SPH, is not necessary employ a SLM with 2π phase modulation. This SLM was configured as a phase-mostly modulator employing a linear polarizer followed by a quarter-wave plate at the input and a second linear polarizer at the output [34], [35], at angles 283^o, 310^o, and 75^o respectively. The phase modulation versus the gray level provided by the SLM illuminated with a He-Ne laser ($\lambda = .6328\ \mu m$) is depicted in Fig. 2.16(b). This phase modulation appears coupled with the amplitude modulation plotted in Fig. 2.16(a).

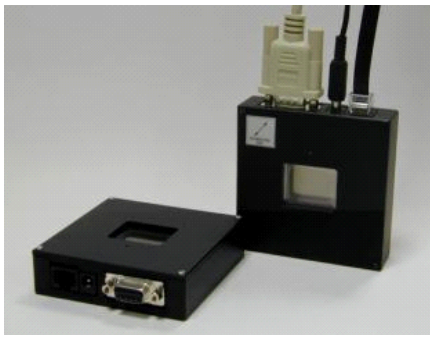

Figure 2.15. LC2002 transmission SLM with 600 x 800 pixels

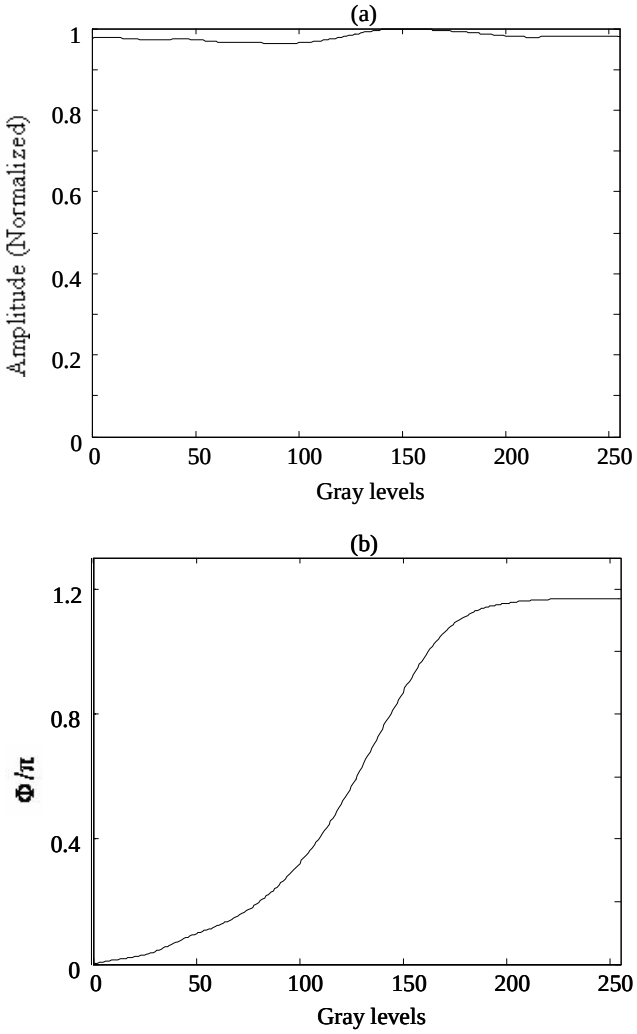

Figure 2.16. Response of the LC2002 SLM to He-Ne laser, (a) Amplitude modulation (Normalized) vs Gray levels, (b) Phase modulation vs Gray levels.

For the design of this type of PSHs the coupled amplitude modulation was neglected. The finite circular support for the encoded beams was chosen with a radius R equal to 100 pixels. Both the radial period r_0 (for Bessel beams Eq. (2.44))) and the waist radius w_0 (for Laguerre-Gauss beams Eq. (2.45)) were adopted as $R/4$.

The Figs. 2.17 and 2.18 show the intensities of the generated Bessel beams of orders $n = 1$ and $n = 3$, respectively.

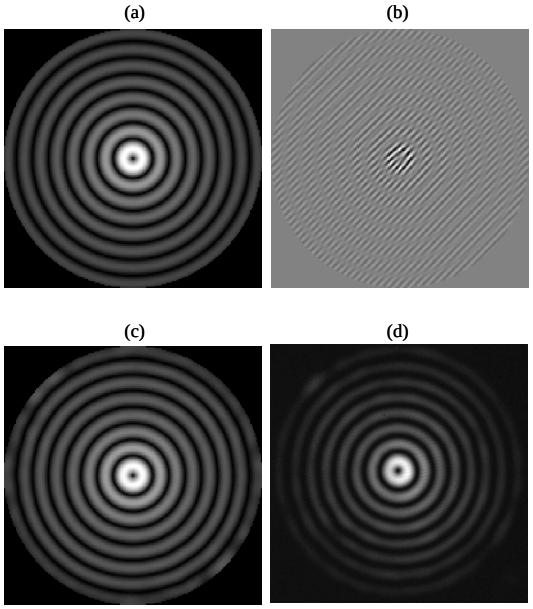

Figure 2.17. Bessel function generated with a support radius R = 100 pixels, r_0 = R/4, and a carrier spatiel frecuency $u_0 = v_0 = \Delta u/6$, n = 1, (a) Source function, (b) Hologram, (c) Theoretical reconstruction, with a SNR = 2.42×10^3, and (d) Experimental reconstruction.

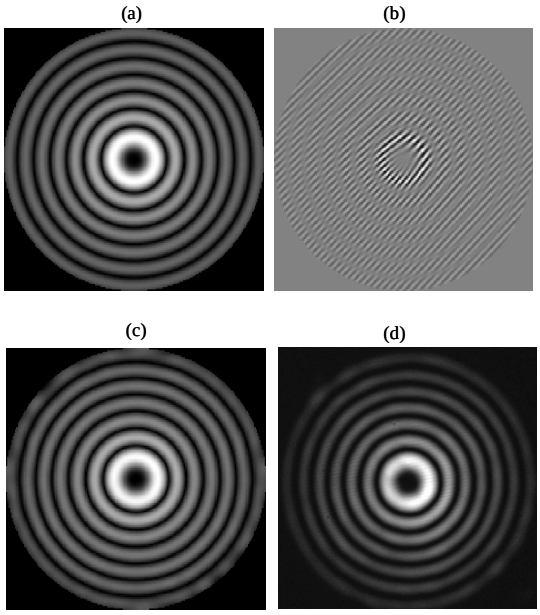

Figure 2.18. Bessel function generated with a support radius R = 100 pixels, r_0 = R/4, and a carrier spatiel frecuency $u_0 = v_0 = \Delta u/6$, n = 3, (a) Source function, (b) Hologram, (c) Theoretical reconstruction, with a SNR = 3.63×10^3, and (d) Experimental reconstruction.

The Figs. 2.19 and 2.20 show the images of the generated Laguerre-Gauss beams with indices (p, l) of (0,2) and (2,4), respectively.

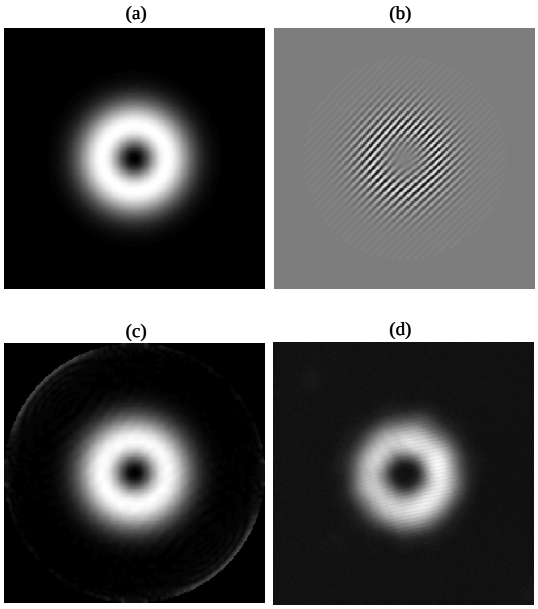

Figure 2.19. Laguerre-Gauss function generated with a support radius R = 100 pixels, r_0 = R/4, and a carrier spatiel frecuency $u_0 = v_0 = \Delta u/6$, (p,l) = (0,2), (a) Source function, (b) Hologram, (c) Theorical reconstruction, with a SNR = 8.43×10^5, and (d) Experimental reconstruction.

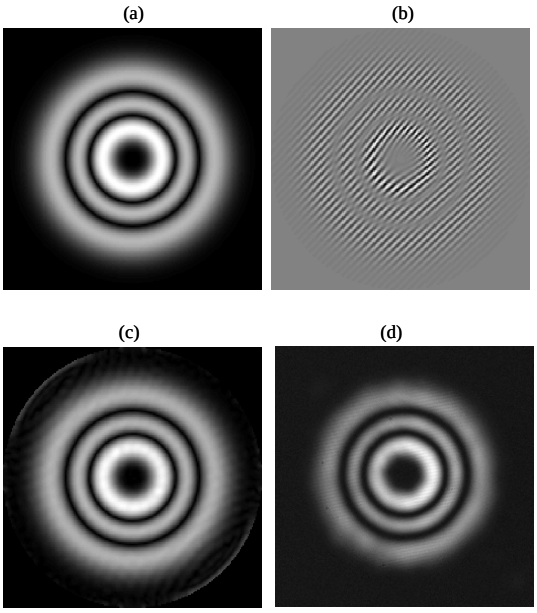

Figure 2.20. Laguerre-Gauss function generated with a support radius R = 100 pixels, r_0 = R/4, and a carrier spatiel frecuency $u_0 = v_0 = \Delta u/6$, (p,l) = (2,4), (a) Source function, (b) Hologram, (c) Theorical reconstruction, with a SNR = 4.95×10^5, and (d) Experimental reconstruction.

The Figs. 2.10-2.13 and 2.17-2.20 show that the generated beams present high SNR even if a pixelated SLM is employed for their implementation. This feature is enabled by the highly attenuated amplitudes of high-order diffraction terms of these SPHs that are expressed in terms of integer-order Bessel functions. The results present a better quality and higher SNR than anothers reported in the literature [20], where the SNRs achieved are low (less than 100). According to the results presented the SPHs type 2 present advantages, respect to the SPHs type 1, because these can be appropiately displayed onto a phase device with a reduced phase range and have a major SNR, however the SPHs type 1 have a major intensity efficiency. Therefore the use of any of them is restricted only by the application.

Chapter 3

Optical tweezers

3.1 Introduction

Optical tweezers is the term used to describe the manipulation of microscopic objects using a single laser beam focused to a diffraction limited spot. In 1986, Ashkin et. al. [36] used a single focused laser beam to stably trap, in three dimensions, particles ranging in diameter from 25 nm to 10 μm in diameter in water. This trapping is due to both the transverse and the axial gradient force exerted by the focused laser beam. An optical tweezer system is a particularly useful tool for biological studies as the trapping process can be completely non-invasive and sterility of samples can be maintained [37].

3.2 Basic forces and the first trap

The first demostration of optical trapping was based on radiation pressure exerted on microparticles, also known as scattering force. To demonstrate it, a 1 W

power laser was focused to a small spot size of about a wavelenght $\cong 1\ \mu m$, and let it hit a particle of diameter also $\sim 1\mu m$. Treating the particle as a 100% reflecting mirror of density $\cong 1\ g/cm^3$, we get an acceleration of the small particle $a = F/m$ $= 10^{-3}\ dynes/10^{-12}\ g = 10^7 G$ (where G is the earth acceleration), for typical trapping forces of some pN., i. e, it is possible to accelerate the small particles several times the earth acceleration. Although, the ligth's momentum is small, it can have a tremendous effect on microparticles.

The first trap consisted of two opposing moderately diverging Gaussian beams focused at points a_1 and a_2 as shown in Fig. 3.1. The predominant effect in any axial displacement of a particle from the equilibrium point E is a net opposing scattering force. Any radial displacement is opposed by the gradient force of both beams. The trap was filled by capture of randomly diffusing small particles which wandered into the trap. The viscous damping of the liquid serves to dissipate all the kinetic energy gained from the random collisions with the liquid molecules and particles come to rest at the trap center. If one beam is blocked, the particle is driven forward and guided by the second beam. If the blocked beam is restored the particle is pushed back to the equilibrium point E, as expected. It is surprising that this simple first experiment, intended only to show forward motion due to laser radiation pressure, ended up demonstrating not only this force but the existence of the transverse force component, particle guiding [38], and stable 3-D particle trapping [36].

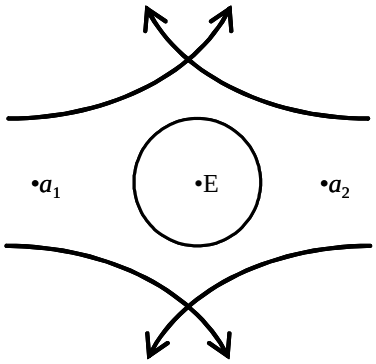

Figure 3.1. Two opposite beams trap

3.3 Forces involved in optical tweezers

Although there are several approaches to study the interaction between the light and the microparticles, here only the two more common regimes will be discussed: Ray optics for particles in the Mie regime (where the particle diameter $d \gg \lambda$) and Rayleigh regime particles ($d \ll \lambda$). Particles in the Rayleigh and Mie regimes compared to λ can be seen in Fig. 3.2.

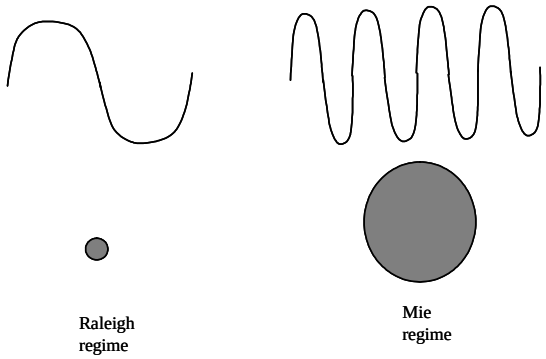

Figure 3.2. Regimes to describe the forces on a particle in optical tweezers

3.3.1 Mie regime

The ray optics aproach is used to calculate forces acting on a particle with a diameter larger than the wavelenght of laser light. The effect of a laser beam on a transparent sphere can be modelled using a bundle of rays, in a similar manner to ray tracing packages that are used for lens design, with each ray weighted according to its intensity. A photon of wavelenght λ has a momentum $p = h/\lambda$ (or $\hbar k$) where h is Plank's constant, and k is the wave number. If an object causes light to change direction, for instance on reflection or refraction, the change in light's momentum will exert an equal but opposite momentum on the object that in turns exert a force on the object given by

$$F = m\frac{d}{dt}(v) = \frac{d}{dt}(mv) = \frac{d}{dt}(p), \tag{3.1}$$

where m represents the object mass and v the velocity. This force exerted on an object is not enough to move macroscopic objects, however, the forces involved in the transfer of momentum from focused laser light can move micron sized particles as was discussed above.

Consider a typical pair of rays **a** and **b** striking the particle symmetrically about its center as shows the Fig. 3.3(a). Neglecting relative minor surface reflections, most of the rays refract through the particle, giving rise to reaction forces $\mathbf{F}_a$ and $\mathbf{F}_b$

towards the opossed direction of the momentum change. Since the intensity of ray a is higher than ray b, the force $\mathbf{F}_{\mathrm{a}}$ is greater than $\mathbf{F}_{\mathrm{b}}$. Adding up all such symmetrical pairs of rays striking the particle, the net force can be resolved into two components $\mathbf{F}_{scat}$ called the scattering force component pointing in the direction of the incident light, and $\mathbf{F}_{\mathrm{grad}}$, a gradient component arising from the gradient in the light intensity and pointing transversely towards the high light intensity region of the beam. For a particle on axis or in a plane wave, $\mathbf{F}_{\mathrm{a}} = \mathbf{F}_{\mathrm{b}}$ and there is no net gradient force component. The reflected (or backscattered) component of the on-axis rays gives rise to radiation pressure and exerts a force on the particle in the direction of beam propagation. This results in the particle being pushed downwards, away from the beam focus.

3-D trapping is the result of the axial gradient force which is created by the tight focusing of the laser beam (Fig. 3.3b). Off-axis rays come in at an angle towards the particle, and these transfer momentum on the particle in the direction of beam propagation. This change in momentum leads to a reaction force which pushes the sphere upwards against the direction of beam propagation towards the focal region of the beam resulting in a trapping force in the z-direction as shows the Fig. 3.3(b), and thus a three dimensional, optical trap. The equilibrium position is reached when the scattering force and gravity (which both act to push the sphere downwards) is

balanced by the axial gradient force (which pushes the sphere upwards) as shows the Fig. 3.3(c).

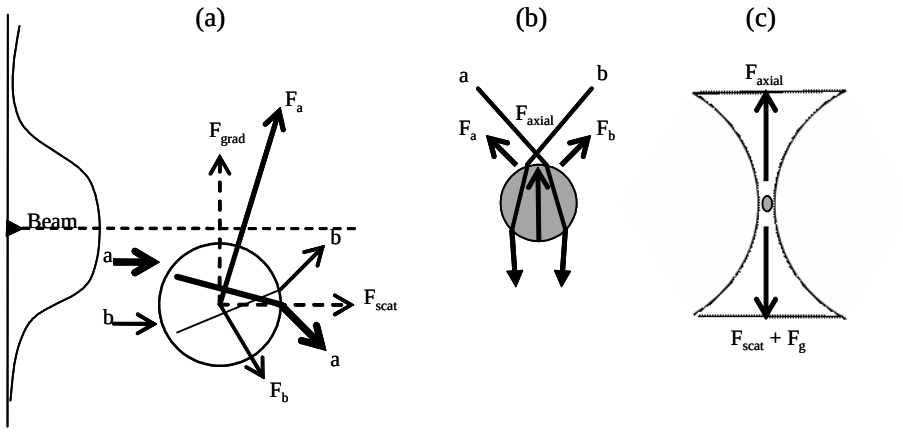

Figure 3.3. Trapping forces on a particle in the Mie regime, (a) Momentum transfer that origin tha forces F_{scat} and F_{grad} ,(b) Axial trapping force, (c) Particle trapped around the area of the highest intensity.

The reader interested on a more detailed calculations of the force are encorage to review the paper of Ashkin [37].

3.3.2 Rayleigh regime

For particles in the Rayleigh regime the ray optics approach can not be used to calculate forces as only a fraction of the wave has an effect on the particle. It is better to consider the force in terms of the electric field in the region of the trapped particle. The forces can be divided into those arising from scattering of the light and those arising from an intensity gradient.

For an object of radius r and light beam of intensity I_0, the force resulting from the light scattering is, [39]

$$\mathbf{F}_{scat} = \frac{I_0}{c}\frac{128\pi^5 r^6}{3\lambda^4}\left(\frac{N^2-1}{N^2+2}\right)^2 n_m \widehat{z}, \tag{3.2}$$

where N is the ratio of the refractive index of the object n to the refractive index n_m of the surrounding medium. Although not apparent from this form of the equation, the scattering force is directed perpendicular to the wavefronts of the incident light, that is objects are pushed in the direction of light propagation.

The intensity gradient near the beam focus gives rise to a gradient force, which is equivalent to the refraction of the rays, given by [39]

$$\mathbf{F}_{grad} = \frac{-n^3 r^3}{2}\left(\frac{N^2-1}{N^2-2}\right)\boldsymbol{\nabla}\left(|E|^2\right). \tag{3.3}$$

Explicit in this equation is that the force is directed towards the region of highest light intensity gradient.

As the scattering force acts along the beam's direction whereas the gradient force acts towards the beam focus, it follows that for a beam directed downwards, the stable trapping point lies just below the focus.

3.4 Typical experimental setup used in optical tweezers

An important factor to consider when using optical tweezers is the profile of the laser beam. TEM_{00} mode Gaussian beams are the most commonly used in optical tweezers systems. The irradiance of a Gaussian beam decreases exponentially towards the edges of the beam and thus provides the transverse optical gradient required to trap particles in a three dimensions.

Stable three dimensional trapping is achieved in a focused laser beam if the gradient force is large enough to overcome the scattering force. This is achieved by using a high numerical aperture (NA) microscope objetive lens, which creates steep gradients due to the angle at which the off-axis rays come into the sample.The numerical aperture equals the refractive index of the immersion fluid, n (air, water or oil), multiplied by the sine of the half angle of opening of the focused light. Angles of opening can be up to 140^o with high numerical apertures having values of 1.0-1.40.

In Fig. 3.4 is shown a typical experimental setup, a telescope may be used to collimate the beam in order to fill up the rear aperture of the microscope objetive. Before entering the microscope objetive aperture, the beam is passed through another pair of lenses in a 1:1 telescope to allow conjugate images to be formed between the beam steering mirror and the back focal plane of the microscope objetive. A dichroic mirror placed at 45^o directs the incident laser beam into the microscope objetive

allowing white light to pass through to form the image of the tweezed particle on the charged coupled device (CCD) camera, the image captured by the CCD camera can be displayed on a monitor and recorded on a video recorder. Incoherent illumination of the sample is provided by a halogen reflector from below the sample cell. A 100x objetive is commonly used to give the smallest possible spot size. Using a less powerful objetive would give a larger spot size at the focus, so the power of the laser is spread over a greater surface and the trap strength is lessened and furthermore, these objetives are not oil immersion microscope lenses.

Sample holders can be created using a microscope slide, a circular hole is done on black scotch tape (150 μm thickness) and placed on top of the microscope coverslip and filled with water containing the particles. A coverslip is used to seal the container. A drop of index-matching oil is placed between the microscope objetive and the coverslip. The sample is placed on a xyz translation stage and, if the beam entering onto the objetive is collimated, then the focus of the beam is coincident with the image plane where the particles lies. The beam can be moved in the sample by changing the angle of the beam steering mirror, or the sample can be moved by translating the xyz on which the sample stage is located.

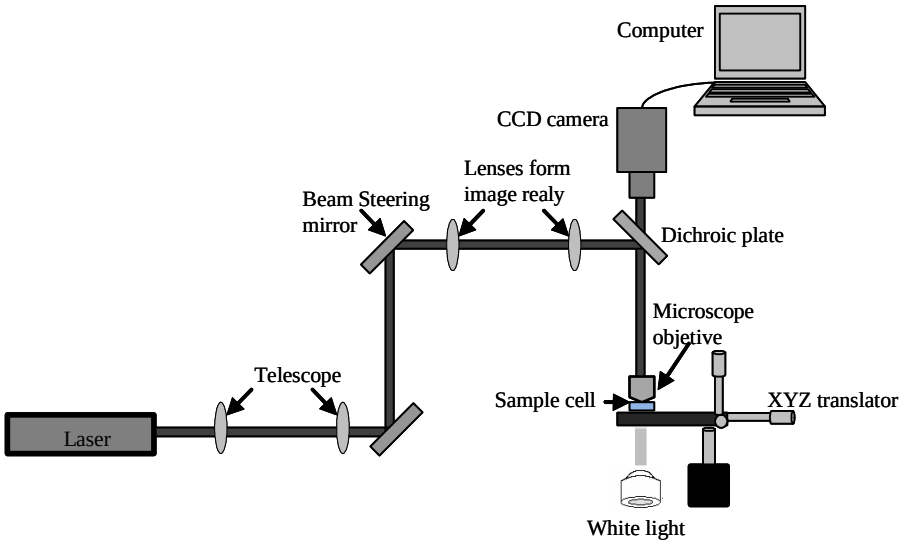

Figure 3.4. System commonly used in optical tweezers

3.5 Particles manipulation using optical forces

This thesis present two applications of manipulation of several particles using SPHs. These SPHs, displayed on SLMs, generate structured light patterns (optical energy landscapes), which can be controled dinamically. Therefore mainly four keys regimes for the manipulation process that combine fluid flow and structured light patterns are briefly discussed below.

3.5.1 Static fluid, static pattern

The most basic form of manipulation exploits the differences in response of the properties of colloidal particles and biological particles to a stationary optical potential energy landscape with no fluid flow present. Motion of objects can be investigated and this is achieved solely by optical forces. How fast the particle moves over the landscape depends on the energy depth of the potential landscape well. Any properties differences would manifest themselves as particle sorting in the absense of flow. Overall, this mean that particles of different size, shape, refractive index, and composition move differently across the optical landscape [**?**], [41]. Also it is possible to use the brownian motion of the particles to achieve a net displacement under the influence of an optical landscape [42]. One of the applications presented below, brownian motion rectification, correspond to this regime.

3.5.2 Dynamic fluid, static pattern

Flowing particles through an optical potential energy landscape will facilitate the manipulation of these objects based on their physical characteristics such as size, shape, and refractive index. Flow through an optical lattice can readily lead to sorting as a function of size or refractive index-related deflection [43], [44].

3.5.3 Static fluid, dynamic pattern

It is possible transport particles employing a dynamic optical landscape. The traveling landscape provides a convenient means of pumping and actuation, but the distance that the particles are carried will depend on many factors, including the shape and extent of the envelope of the optical pattern itself: as the intensity in the pattern falls off more strongly, interacting particle species will be carried further than those that respond weakly to the optical forces [45]. Since this dynamic phase of operation does not have a fluid flow to remove sorted particles, particles will accumulate at the position for which the optical conveyor belt is no longer strong enough to transport them, leading to a fractionated column of different particle species which may then be extracted [46]. The other application presented in this thesis correspond to this regime.

3.5.4 Dynamic fluid, dynamic pattern

The final regime utilizes a motional light pattern within a microfluidic flow. To date, this is a little explored regime even though it offers more degrees of fredom with respect to tuning the manipulation process. A particular advantage of this combination is that deflected particles can be moved out of the polydisperse flow more quickly, leading to fewer particle-particle interactions that might otherwise lead to undesirable behavior of the particles (clustering, jamming, incomplete deflection, or

separation). This will allow higher efficiencies to be achieved in the sorting process [47].

In the next chapter are presented two applications of SPHs, implemented in SLMs, that generate structured light patterns. These structured light patterns allow the manipulation of several particles. To generate this patterns is employed a type of SPH called iterative Fourier transform algorithm (IFTA) [48], this IFTA is chosen because for the applications presented, we only need a SPH that control the intensity distribution, while the phase of the pattern can be random. Also the IFTA present a high intensity efficiency ($\approx$80%) compared with others SPHs.

Chapter 4

Computer generated holograms applied to microparticles manipulation

In this thesis, we show the experimental manipulation of several particles using optical lanscapes without fluid flow. One of the applications presented below is based in the generation of a dynamic spot array pattern. This pattern generate a set of multiple traps, which allows the trapping of microparticles. Moving the pattern is possible separate particles, according to the characteristics of these traps (diameter, intensity). The other application presented below is based in the brownian motion of particles (flashing ratchets). This technique allows the manipulation of nanoparticles because with the conventional techniques, of manipulation, is very difficult achieve traps with diameters so small.

4.1 Iterative Fourier transform algorithm

IFTA is a technique that can solve the following problem: designing a CGH that will convert a light field $E_0(\overrightarrow{r})$ at the CGH, or input plane, into a target intensity

distribution $I_0(\overrightarrow{\rho})$ at the focal plane of a focusing optic. The light field $E_0(\overrightarrow{r})$ is typically a Gaussian beam apodized by the input aperture of the device used to implement the CGH. The IFTA problem does not have a unique solution, as the complex phase of the optical field associated is not constrained. This is known as phase freedom: there is a choice of phase in the output plane [49], [48]. An IFTA is designed to use phase freedom to minimize the difference between $I_0(\overrightarrow{\rho})$ and the intensity distribution produced by the CGH in the output plane.

An IFTA can be decomposed into two parts as illustrated in Fig. 4.1: an initialization step and an iterative loop. In the initialization step, a phase distribution $\phi_0(\overrightarrow{r})$ is chosen as a starting point for the algorithm and is imprinted on $E_0(\overrightarrow{r})$ to produce the input field $E_{in}^{(1)}(\overrightarrow{r}) = A_0(\overrightarrow{r}) \exp\left[i\phi_0(\overrightarrow{r})\right]$ for the first iteration. Each iteration n of the loop begins calculating the field $E_{out}^{(n)}(\overrightarrow{\rho}) = \mathcal{F}\left\{E_{in}^{(n)}(\overrightarrow{r})\right\}$ produced by $E_{in}^{(n)}$ propagating to the output plane.

The propagation is carried out using a Fourier transform $\mathcal{F}$, which assumes the paraxial approximation for the focusing optics [50]. The algorithm then combines the propagated field $E_{out}^{(n)}$ with the target intensity profile I_0 to produce a new field $G^{(n)}(\overrightarrow{\rho})$. This procedure is carried out using one or more numerical scalars called mixing parameter m. The phase of the backward propagated field $\arg\left\{\mathcal{F}^{-1}\left[G^{(n)}\right]\right\}$ is used as the starting phase distribution for the next iteration.

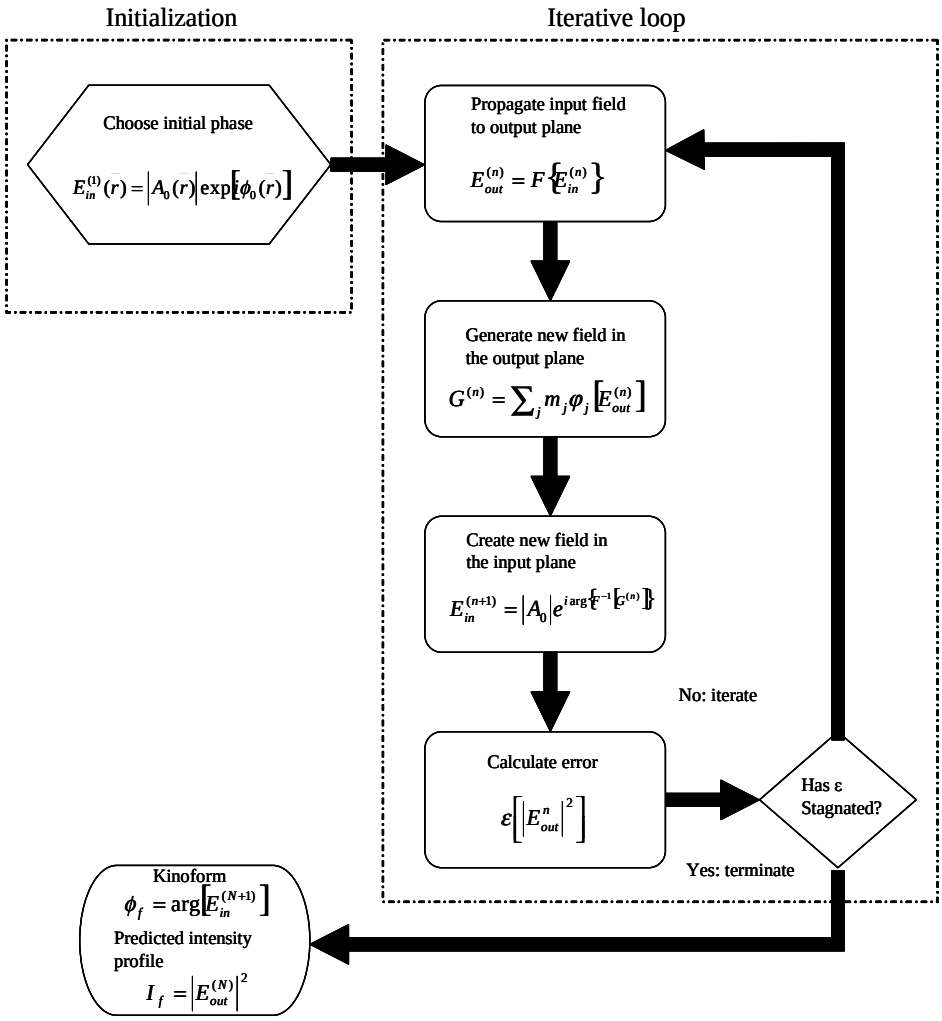

Figure 4.1. IFTA flow chart

The iterative loop is terminated after N iterations once the error ε, calculated using the intensity profile in the output plane and I_0, does not improve with repeated iterations. The phase profile $\phi_f(\overrightarrow{\rho}) = \arg\left[E_{in}^{(N+1)}\right]$ of the field in the input plane for the final iteration is the kinoform which must be transferred to a physical device.

The SPHs generated with the IFTA were implemented on a phase-only SLM, to obtain the results presented in the next sections.

4.2 Sorting particles

The sorting particles is a technique that plays an important role mainly in biology and medicine. Although, there are several techniques of sorting, here we will only give a brief description of some techniques that use optical landscapes without fluid flow. The use of different complex fields, as Bessel beams, have been employed to manipulate microparticles. Due to the "diffraction free" property of the Bessel beams [51], they have been exploited for long range optical guiding of microparticles [52]. Moreover the Bessel beams, also have interesting features relating to equilibria positions for trapped objects that depend on the physical parameters, therfore this type of beams have been employed to sort particles [53].

Others techniques where the sorting is achieved with a dynamic optical landscape have been investigated. A vibrating fringe pattern has been used to move and separate colloidal particles [54]. A Mach Zender interferometer type arrangement was used to generate a sinusoidal fringe pattern projected into the sample plane of the trap. One of the mirrors in the interferometer vibrated using a piezoelectric mount and caused the fringe pattern to oscillate in a sawtooth-like manner in one direc-

tion. The size effect was employed to separate 2 and 5 μm polystyrene particles. Moreover, it was also possible to separate particles of the same size (5 μm) made of polystyrene and silica, thus showing sorting based on refractive index variations.

A more advanced method to generate 2D or 3D dynamically reconfigurable landscapes is to use the SLMs [55], [56]. They work as a phase grating (hologram) where each pixel can be independiently addressed so that it has different optical thickness or converting amplitude to phase using the generalized phase contrast method [57], [58]. This tool can generate motional periodic light patterns with direct applications to the flow-free particle motion termed optical peristalsis [59]. Then we present the experimental realization of sorting particles using a dynamical optical landscape, which is generated with a SLM. In order to achieve particle sorting, it is necessary to project a sequence of spatially displaced array. The optimum displacement depends on the array's dimension, Fig. 4.2 schematically depicts how optical sorting works.

At the onset of each cycle, a particle is localized on one optical potential well. Several such wells form a pattern that covers the whole field of view. In Fig. 4.2(a), two wells are represented schematically by two Gaussian optical traps. Replacing the first pattern with another laterally displaced, transfers the particle onto the nearest well of the new pattern. Subsequently displacements transfer the particle once again. Because the array can cover the entire field of view, transporting a particle, in this manner does not require active tracking. The advantage of this system is that no

microfluidic flow is need to sort particles as other systems [43] and it is much simpler and robust that phase-modulated interferometric systems [54].

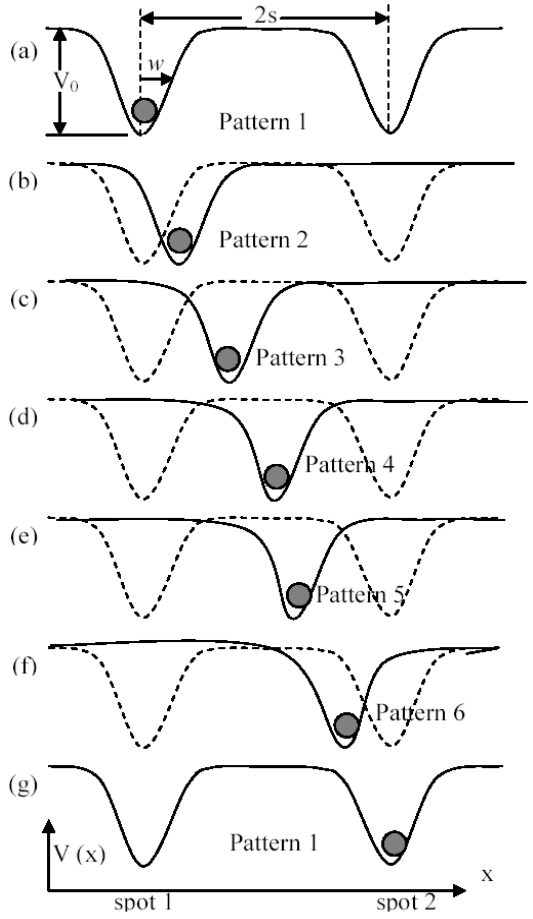

Figure 4.2. (a) through (g) show one cycle through six distinct states of a spatially symmetric optical pattern. A particle in one well is transferred to the next by the end of the cycle.

4.2.1 Experimental results

Here is present a dynamic spot array pattern, to sort particles, where no fluid flow is employed. The periodic phase grating, that generates the spot array, is ob-

tained by mean of an IFTA [18]. The separation between spots of the array is given by $s = \lambda f / p$, where λ is the laser wavelenght, f is the lens focal distance used to generate the spot array in the Fourier plane, p is the period of the grating.

An array of 3 x 5 spots was used with separation $2s$ in the horizontal direction as show in Fig 4.3(b). A $5W$ solid state laser Verdi with a wavelength of $532nm$ was employed to illuminate the SPH, shown in Fig. 4.3(a), displayed on a Boulder non linear system SLM. The period of the phase grating was $0.96mm$ ($64\delta x$), the focal distance of the lens was 60 cm (which was codified on the SPH), so the separation between spots was $s = 0.33mm$.

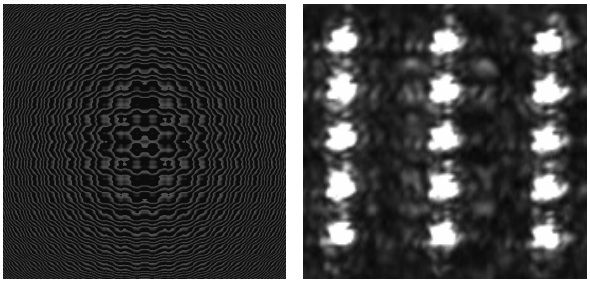

Figure 4.3. Experimental image of a 3 x 5 spot array

The size and shape of the each spot is determined by the SLM illuminating pupil ($b(x, y)$), since the Fourier's transform consists of the product between the illuminating pupil and the periodic grating (t). The array of spots is represented by a set of delta functions centered at the diffraction orders (q, l), i.e.

$$\mathcal{F}\{b \cdot t\} = \mathcal{F}\{b\} * \mathcal{F}\{t\} = B(u,v) * \delta(u-q, v-l) = B(q,l). \tag{4.1}$$

The experimental setup is shown in Fig. 4.4. Here SF is a spatial filter (diaphragm) to filter the Fourier spectra, RL is a relay lens that projects the array pattern into a 100x oil-immersion microscope objective (O), SLM is the phase-only spatial light modulator, DP is a dichroic plate, P is a cell with the particles mixture, IS is an incoherent illuminating source that project the particles image into the charged couple device (CCD). The overall hologram efficiency, including computer-designed diffraction grating and the diffraction efficiency of the SLM, is roughly 30%.

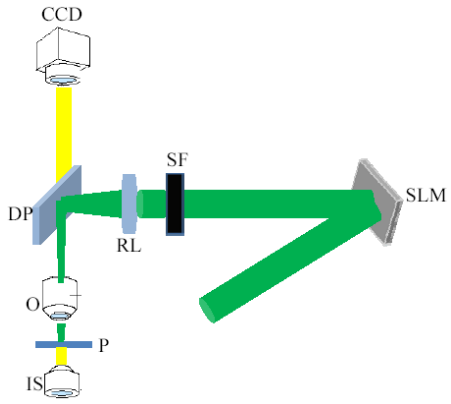

Figure 4.4. Experimental setup for sorting particles

For the experimental conditions, the size of each spot in the pattern projected at the trapping plane was approximately $w = 1.7\mu m$ and the separation in the horizontal direction between spots is $6.6\mu m$. A mixture of particles of $5\mu m$ and $2\mu m$ diameter was placed on the cell.

Sorting of particles ($5\mu m$ and $2\mu m$ diameter) is shown in the Fig. 4.5. The power of each spot is approximately $8mW$ and the rate cycle is $2Hz$. From the Fig 4.5. can be noticed that for high density of particles, van der Waals forces causes them to form cluster of particles which limits the maximum speed of the particles. For low density of particles it is possible achieve velocities as high as $30\mu m/seg$, comparable with the fasted methods reported so far. Increasing the power of the individual traps can lead to even higher velocities. However the laser power did not increase above 1 W to avoid damage to the SLM. In Fig. 4.5, an average velocity of $4.9\ \mu m/s$ is achieved due to the formation of 2-3 particles clusters []. Sorting of particles ($5\mu m$ and $1\mu m$ diameter) is shown in the Fig. 4.6. The power of each spot is approximately $4mW$ and the rate cycle is $2Hz$. An average velocity of $2.7\ \mu m/s$ is achieved.

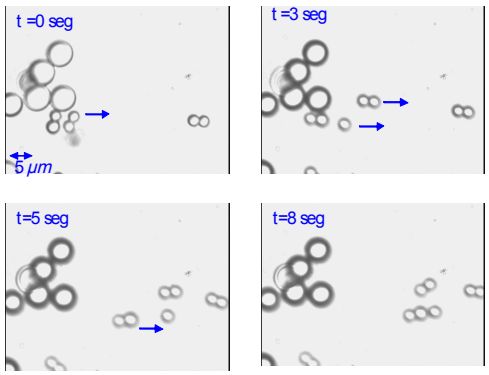

Figure 4.5. Sorting particles of 5 μm and 2 μm. Each frame was captured at different times.

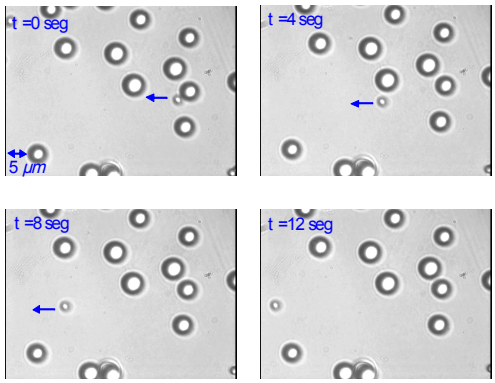

Figure 4.6. Sorting particles of 5 μm and 1 μm. Each frame was captured at different times.

4.3 Brownian motion rectification

Recently, noise-induced anomalous transport phenomena of Brownian particles in periodic structures has surge as hot research topic. In particular, ratchet effect i.e., a directed motion of Brownian particles induced by nonequilibrium fluctuations, with no macroscopic driving force applied, in spatially periodic structures it has attracted a lot of attention. In fact, the ratchet effect has been demonstrated experimentally by using microelectrode devices [61] and optical traps [42]. One of the main disadvantages of such systems is the need of large applied electric field and the physical structuring of the device or the low throughput of the system.

Ratchets allow the rectification (directed transport) microparticles due to thermal fluctuations. Apart from transients, directed transport in a spatially periodic system in contact with a single dissipation- and noise-generating thermal heat bath

is ruled out by the second law of thermodynamics. The system has therefore to be driven away from thermal equilibrium by an additional deterministic or stochastic perturbation. Most of the rectifiers or Brownian ratchets work by introducing an external time-dependent perturbation in an asymmetric equilibrium system. In case of rocking ratchets, the perturbation is an AC uniform field, whereas for the flashing ratchet [62], [63] the perturbation consist of switching on and off an asymmetric sawtooth potential as show the Fig. 4.7.

4.3.1 Basic theory of flashing ratchets.

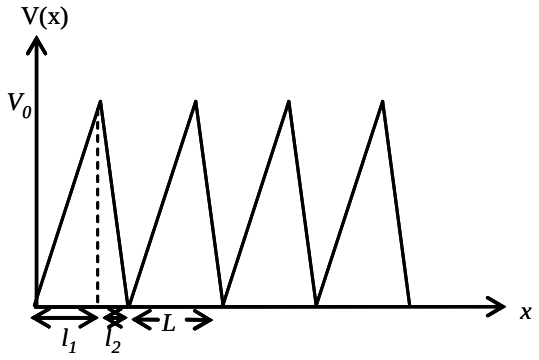

Figure 4.7. Sawtooth potential with perid L.

In the context of flashing ratchet consider an ensemble of N overdamped Brownian particles at temperature T in an external asymmetric periodic potential $V(x)$, that can be either on or off. The dynamics is described by the Langevin equation [64]

$$\gamma \dot{x_i}(t) = \alpha(t) F\left(x_i(t)\right) + \xi_i(t), \qquad i = 1.....N, \tag{4.2}$$

where $x_i(t)$ is the position of particle i, γ is the friction coefficient and $\xi_i(t)$ are thermal noises with zero mean and correlation $\left\langle \xi_i(t)\xi_j(t')\right\rangle = 2\gamma^2 D\delta_{ij}\delta(t-t')$, where D is the diffusion coefficient. The force is given by $F(x) = -V'(x)$ where $V(x)$ is defined by

$$V(x) = \begin{cases} \frac{V_0 x}{l_1 L} & \text{if} \quad 0 \leq \frac{x}{L} \leq l_1 \\ -\frac{V_0}{(1-l_1)}\left(\frac{x}{L} - l_1\right) + V_0 & \text{if} \quad l_1 \leq \frac{x}{L} \leq 1 \end{cases}, \tag{4.3}$$

$\alpha(t)$ is a control parameter which is assumed that can take on the values 1 and 0, i.e., the only allowed operations on the flashing ratchet consist of switching on and off the potential $V(x)$. It is possible consider the following two switching strategies:

1.-Periodic switching: $\alpha(t+\tau) = \alpha(t)$, with $\alpha(t) = 1$ for t $\in$ [0, τ/2), and $\alpha(t) = 0$ for t $\in$ [τ/2,). This case is equivalent to the periodic flashing ratchet [65].

2.-Controllled switching

$$\alpha(t) = \Theta(f(t)) \qquad \text{with} \qquad f(t) = \frac{1}{N}\sum_{i=1}^{N} F\left(x_i(t)\right), \tag{4.4}$$

where $f(t)$ is the net force per particle and $\Theta(y)$ is the Heaviside function, $\Theta(y) = 1$ if $y \geq 0$ and 0 otherwise. Particles are no longer independent, due to the feedback control $\Theta(y)$.

By employing the controlled switching strategy, when on the potential (τ_{on}), the particle is confined in a potential minimum. when off the potential (τ_{off}), the particle now diffuses freely. For small τ_{off}, the particle does not have enough time to diffuse to the next minimum and stay in the same well. For large τ_{off} the particle diffuses to the forward or backward minimum with equal probabilty 1/2. The forward probability can be described by [61]

$$P_f = \frac{1}{2}\exp(-\tau_f \diagup \tau_{off}), \tag{4.5}$$

where τ_f is the average time for the particle to diffuse a distance d_f, $\tau_f = d_f^2 \diagup 2D$. In a similar way the backward probability is approximated by [61]

$$P_b = \frac{1}{2}\exp(-\tau_b \diagup \tau_{off}), \tag{4.6}$$

where the characteristic time is equal to $\tau_b = d_b^2 \diagup 2D$.

As an example the Fig. 4.8 shows the diffusive probabilities (P_f and P_b), assuming the diffusion coefficient of a 0.5 μm particle ($D \approx 1.028 \mu m^2/\sec$), $d_f = 1\mu m$ and $d_b = 4\mu m$.

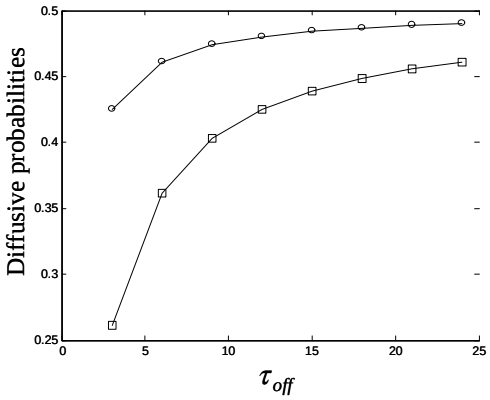

4.8. Diffusive probabilities vs diferents off times, P_f (circles), P_b (squares).

The Fig. 4.8 shows that, with the parameters chosen, the particle have a major forward probability. Therefore after several cycles (turning on and turning off) the particles will have a net displacement in one direction. Employing this principle we show the brownian motion rectification, althoug it had been demonstrated by Fauchuex et al. [42], they only achieved brownian motion rectification to one particle. Here we demonstrate experimentally the brownian motion rectification by several particles.

4.3.2 Experimental results

In order to produce the flashing ratchet an IFTA algorithm [19] was used to generate a spatial sawtooth potential. This potential is periodic but spatially asymmetric and deep enough to trap the particles (energy larger than the thermal energy at room temperature). The 9 periods fill the field of view (30x24 μm^2). Theoretically,

an efficiency power around 70% and an error around 15% is obtained. The CGH is shown in Fig. 4.9(a). The CGH generated is displayed into of a spatial phase light modulator from Boulder Nonlinear Systems. Unfortunately this device presents diffraction efficiency around 40%, and no uniform modulation over its active area, so that experimentally the CGH has a maximum efficiency power around 30%. The experimental pattern is shown in the Fig. 4.9(b) and the Fig. 4.9(c) shows the average transverse profile of the sawtooth potential. Although the experimentally generated hologram is not perfect it works fine to achieve the brownian motion rectification.

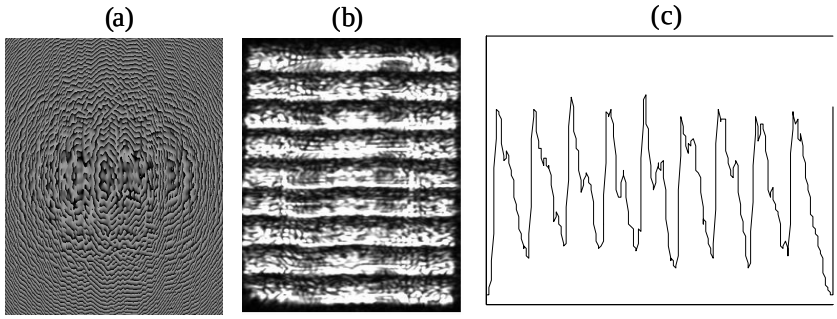

Figure 4.9. (a) SPH that generates the sawtooth potential, (b) Experimental image of the sawtooth potential, (c) Average tranverse profile of the sawtooth potential.

A Verdi 5 solid state laser with a wavelength of $532nm$ was used to illuminate the SPH displayed onto the spatial light modulator (SLM). Fig. 4.10 shows the experimental setup. A collimated and spatially filtered laser beam illuminates the SLM, after reflection, the beam is phase modulated carrying the information of the hologram and reconstructed, after reflection on a dichroic mirror, on the focal plane of the 100x objective lens. Illumination with an incoherent source is used to project the

particles image onto a CCD camera. To avoid damage to our phase modulator, the maximum power launched was 700 mW, which produced about 200 mW of power at the focal plane.

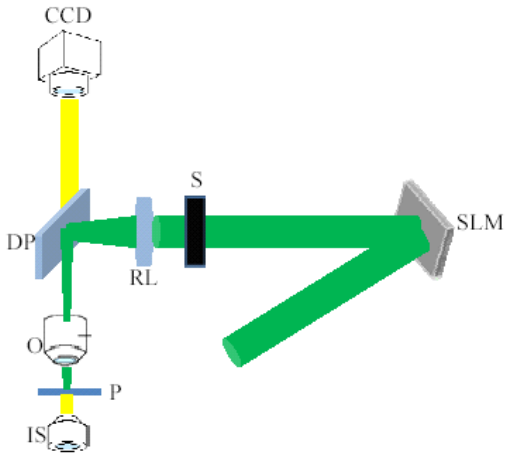

Figure 4.10. Experimental setup employed for brownian motion rectification.

The principle of operation of the flashing ratchet is shown in Fig. 4.11. When the potential is on, the particles are trapped in the potential minima, assuming that the potential energy is larger than the thermal one. When the potential is off, then the particles freely diffuse. If the off time is not long enough, then the particle will diffuse for a distance r not larger than the spatial period of the potential (L). The distance that the particles move is equal to $r = (4Dt_{off})^{1/2}$, where D is the diffusion coefficient, with equal probability of moving to the left than to the right. Once the potential is on again, the particles that had moved to the right are returned to the potential minima but the ones that moved to the left are trapped to the next potential minimum. In this way, rectification of the Brownian motion is obtained.

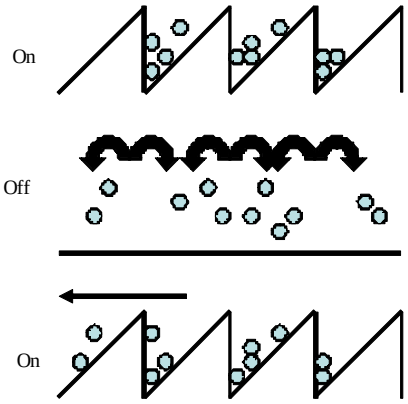

Figure 4.11. Principle of operation of flashing ratchets.

Colloidal 0.5 $\mu m$and 1μm silica particles were used to fill up a 100 μm thick cell. The rectification of the Brownian motion was achieve using the potential shown in Fig. 4.9(b), which has 9 periods of 3.5 μm approximately each one. Turning on (t_{on}) and turning off (t_{off}) the potential, the average velocities (v_{av}) obtained are shown in Fig. 4.12. The on time was kept fix and the off time was varied (1sec - 4sec). It was found that a t_{0ff} of 1 sec optimizes the average velocity of the particles.

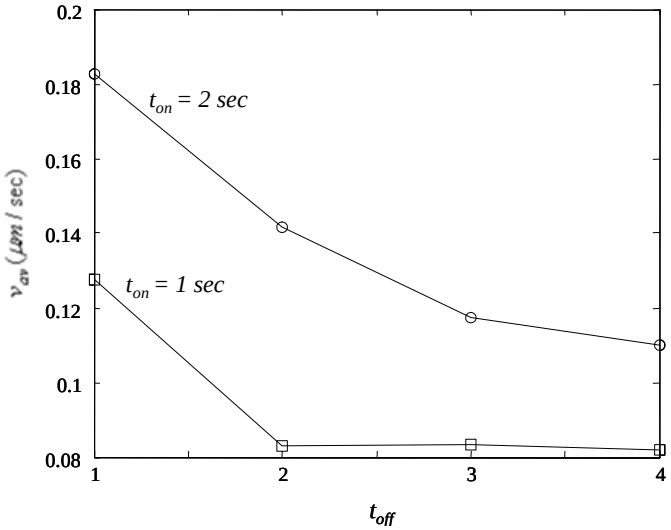

Figure 4.12. Average velocities versus turn off time, (circles) represent a turn on time of 2 sec, and (squares) represent a turn on time of 1 sec.

A set of 10 particles were tracked using the free software IMAGEJ which allows to measure the velocity of the each particle. A directed current is generated downwards with an average velocity of $0.1\mu m/sec$, as is shown in the Fig. 4.13. This velocity compares with the one obtained using dielectrophoretic ratchets [66].

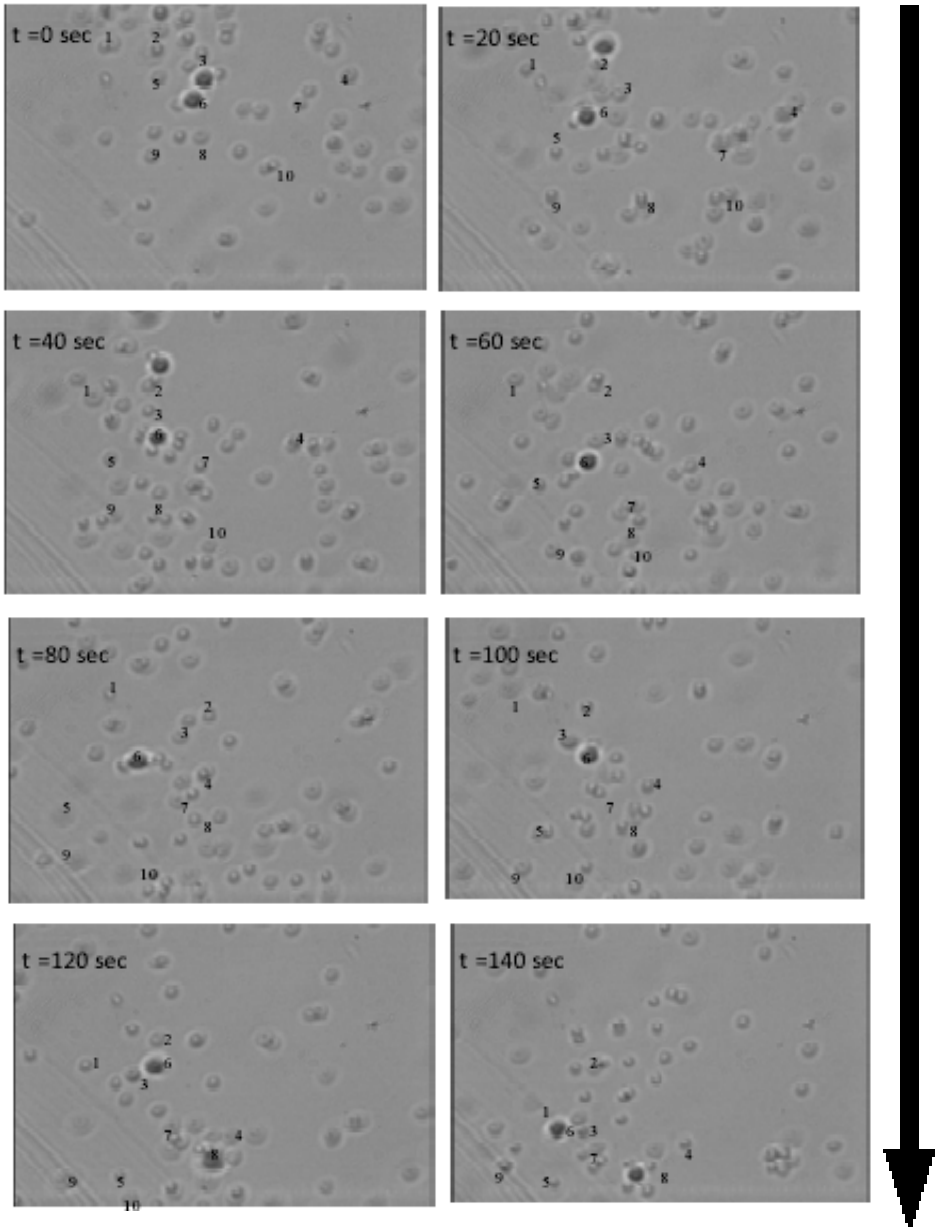

Figure 4.13. Experimental flashing ratches, the particles sizes of the mixture is 1 μm and 0.5 μm.A set of 10 particles is checked to show the brownian motion rectification.

Chapter 5

Conclusions

In this thesis has been discussed a class of SPHs to codify arbitrary scalar complex fields [33]. It has specified the conditions that a SPH of this class must fulfill to encode the complex field. The two novel types of SPHs presented allow reconstruction with a relatively high SNR even if a pixelated SLM is employed for their implementation. Moreover, one of the proposed holograms can be appropiately displayed onto a phase device with a reduced phase range.

It was presented the experimental synthesis of Laguerre- Gauss and nondiffracting Bessel beams of some orders employing a reflective phase SLM for the SPH type 1 and a transmission twisted-nematic LC SLM in a phase-mostly configuration that provided a phase range of approximately 1.2π for the SPH type 2. The SPHs type 2 present a better SNR than the SPHs type 1, also the SPHs type 2 have the advantage of can be implemented with a reduced phase response. However the SPHs type 2 have lower intensity efficiency than the SPHs type 1.

Additionally to the SPHs reported in the thesis, we recently have developed others SPHs, one of these can generate nondiffracting Bessel beams with high SNR

and intensity efficiencies higher than 70% [67]. The other SPH developed can generate multiple beams [68].

It was presented sorting of microparticles. In order to sort microparticles was employed a dynamical spot array pattern without fluid flow, this pattern is formed by a holograms's sequence that are displayed to determined frequency, so that, it was achieved sorting of particles, 1 μm and 5 μm in one case, and 2 μm and 5 μm in another case. The average velocities achieved were about 4.7 $\mu m/\sec$, but it were achieved individual velocities as high as 30 $\mu m/\sec$ [60].

Also it was shown rectification of Brownian motion employing the flashing ratchet technique. This technique allows to employ the thermal fluctuations to achieve a particles current, in a preferred direction, applying a spatial asymmetric light pattern (sawtooth potential). Average velocities about 0.2 $\mu m/\sec$ were achieved taking turning on and off times determined.

Publications

1.- V. Arrizón, U. Ruiz, R. Carrada, and L. A. González, "Pixelated Phase Computer Holograms for the Accurate Encoding of Scalar Complex Fields," J. Opt. Soc. Am. A 24, 3500-3507 (2007)

2.- V. Arrizón, Sabino Chávez-Cerda, Ulises Ruiz and Rosibel Carrada, “Periodic and Quasi-periodic Non-diffracting Wave Fields Generated by Superposition of Multiple Bessel Beams”, Optics Express, Vol. 15, No. 25, 2007.

3.- V. Arrizón, U. Ruiz, G. Mendez, and A. Apolinar-Iribe, “Zero Order Synthetic Hologram with a Sinusoidal Phase Carrier for Generation of Multiple Beams”, Opt. Express, Vol. 17, p. 2663-2669, 2009.

4.- V. Arrizón, D. Sanchez-De la Llave, U. Ruiz, and G. Mendez, “Efficient Generation of an Arbitrary Non-diffracting Bessel Beam Employing its Phase Modulation”, Opt. Lett., Vol. 34, p. 1456-1458, 2009.

Proceedings

1.- Ulises Ruiz and Victor Arrizzon “Characterization of Twisted Liquid Crystal Spatial Light Modulators”, VI Simposium la òptica en la industria, Monterrey Nuevo León, México, March 2007.

2.- Victor Arrizon, Ulises Ruiz, Rosibel Carrada y Luis A. González, “Accurate Encoding of Complex Optical Fields with Pixelated Phase-only Spatial Light

Modulators", Sixth Euro American Workshop on Information Optics at Grand Hotel Reykjavik, Iceland, 25 – 30 June 2007.

3.- Ulises Ruiz, Victor Arrizon, J. Cesar Ramirez and Rubén Ramos, "Sorting of Microparticles by Optical Landscapes Displayed on a Spatial Light Modulator", SPIE OPTICS AND PHOTONICS, San Diego, California, USA, August 2008.

4.- Ulises Ruiz, Victor Arrizon, Nicolai Korneev and Rubén Ramos "Brownian Motion Rectification of Micro Particles Applying an Asymmetrical Optical Potential", XXI Annual Meeting in Optics, Zacatecas, Zacatecas, México, October 2008.

References

[1] D. Gabor, “A New Microscope Principle,” Nature, Vol. 161, p. 777, 1948.

[2] H. John Caulfield, The Art and Scienceof Hologrphy, SPIE Press., 2004.

[3] Theodore Maiman, “Stimulated Optical Radiation in Ruby,” Nature, Vol. 187, p. 493-494, 1960.

[4] E. N. Leith and J. Upatniek, “Reconstructed Wavefront and Communication Theory,” J. Opt. Soc. Am., Vol. 52, p. 1123, 1962.

[5] M. G. Lippmann, “La photographie des coulers,” Comp. Rend., Vol 112, p. 274, 1891.

[6] Y. N. Denisyuk, “Photographic Reconstruction of the Optical Properties of an Object in its Own Scattered Radiation Field,” Sov. Phys. Doklady, Vol. 7, p. 543, 1962.

[7] B. R. Brown and A. W. Lohmann, Appl. Opt., Vol. 5, p. 967, 1966

[8] A. W. Lohmann and D. P. Paris, “Binary Fraunhofer Hologrmas, Generated by Computer,” Appl. Opt., Vol. 6, pp. 1739-1748, 1967.

[9] Wai Hon Lee, “Sampled Fourier Transform Hologram Generated by Computer,” Appl. Opt., Vol. 9, pp. 639-643, 1970.

[10] J. J. Burch, “A Computer Algorithm for the Síntesis of Spatial Frequency Filtres,” Proc. of IEEE, Vol. 55, pp. 599-601, 1967.

[11] J. C. Wyant and V. P. Benett, “Using Computer Generated Holograms to Test Aspheric Wavefronts,” Appl. Opt., Vol. 11, pp. 2833-2839, 1972.

[12] Wai Hon Lee, “Holographic Grating Scanners with Aberration corrections,” Appl. Opt., Vol. 16, pp. 1392-1399, 1977.

[13] Antii Vasara, Jari Turunen, and Ari T. Friberg, “Realization of General Con-diffracting Beams with Computer-Generated Holograms,” JOSA A, Vol. 6, pp. 1748-1754, 1989.

[14] Norbert Streibl, ”Beam Shaping with Optical Array Generators,” J. of Modern Optics, Vol. 36, pp. 1559-1573, 1989.

[15] R. Carrada and V. Arrizon, "Implementation of Complex Transmittances with a Phase Electro-Optical Modulator," Proc. of SPIE, Vol. 6422, 2007.

[16] V. Arrizón, S. Chavez-Cerda, U. Ruiz, and R. Carrada,"Periodic and Quasi-Periodic Non-Diffracting Wave Fields Generated by Superposition of Multiple Bessel Beams," Opt. Express, Vol. 15, pp. 16748-16753.

[17] Jeffrey A. Davis, Mark J. Mitry, Miguel A. Bandres, Isaac Ruiz, Kevin P. McAuley, and Don M. Cottrell, "Generation of Accelerating Airy and Accelerating Parabolic Beams using Phase-Only Patterns," Appl. Opt., Vol. 48, pp 3170-3176, 2009.

[18] V. Arrizon, M. Testorf, S. Sinzinger, and J. Jahns, “Iterative Optimization of Phase-Only Diffractive Optical Elements Based on a Lenslet Array,” J. Opt. Soc. Am. A, Vol. 17, p. 2157–2164, 2000.

[19] M. Pasienski and B. DeMarco, “A High-Accuracy Algorithm for Designing Arbitrary Holographic Atom Traps,” Opt. Express, Vol. 16, p. 2176, 2008.

[20] J. A. Davis, D. M. Cottrell, J. Campos, M. J. Yzuel, and I. Moreno, “Encoding Amplitude Information onto Phase-Only Filtres,” Appl. Opt., Vol. 38, pp. 5004-5013, 1999.

[21] Joseph W. Goodman, *Introduction to Fourier Optics*, Roberts & Company Publishers Third Edition.

[22] Pochi Yeh and Claire Gu, *Optics of Liquid Crystal Displays*, John Wiley & Sons. Cambridge University Press 1984.

[23] U. Ruiz and V. Arrizon, "Characterization of twisted liquid crystal spatial light modulators," Proc. of SPIE, Vol. 6422, 2007.

[24] Robert Guenter, *Modern Optics*, John Wiley & Sons.

[25] P. Hariharan, *Optical Holography*, Cambridge University Press 1996.

[26] G. N. Watson, *A treatise on the theory of Bessel functions,* Cambridge University Press, p. 22.

[27] W. H. Lee, "Computer-Generated Holograms: Techniques and Applications", In Progres in Optics, Vol. 16, p. 121-232, 1978

[28] L. P. Yaroslovskii and N. S. Merzlyakov, *Methods of Digital Holography*, New York: Consultans Bureau, Plenum Publishing Co., 1980.

[29] W. J. Dallas, "Computer-Generated Holograms," In the Computer in Optical Research, Topics in Applied Physics, Vol. 41, p. 291-366, 1980.

[30] W. T. Cochran, J. Cooley, D. L. Favin, H. D. Helms, R. A. Kaenel, W. W. Lang, G. C. Maling Jr., D. E. Nelson, C. M. Rader, and P. D. Welch, "What in the First Fourier Transform?," Proc. IEEE, Vol. 55, p. 1664-1674, 1967.

[31] V. Arrizón, G. Méndez, and D. Sánchez-de-La-Llave, "Accurate Encoding of Arbitrary Complex Fields with Amplitude-Only Liquid Crystal Spatial Light Modulators," Opt. Express 13, 7913–7927 (2005).

[32] V. Arrizon, U. Ruiz, R. Carrada, and L. A. Gonzalez, "Accurate Encoding Of Complex Optical Fields With Pixelated Phase-Only Spatial Light Modulators," 6^{th} International Workshop on Information Optics, 2007.

[33] V. Arrizón, U. Ruiz, R. Carrada, and L. A. González, "Pixelated phase computer holograms for the accurate encoding of scalar complex fields," J. Opt. Soc. Am. A, Vol. 24, pp. 3500-3507, 2007.

[34] R. Ponce, A. Serrano-Heredia, and V. Arrizón, “Simplified Optimum Phase-Only Configuration for a TNLCD,” Proc. SPIE 5556, p. 206–213, 2004.

[35] H. Kim and Y. H. Lee, “Unique Measurement of the Parameters of a Twisted-Nematic Liquid-Crystal Display,”Appl. Opt., Vol. 44, p. 1642–1649, 2005.

[36] A. Ashkin, J. M. Dziedzic, J. E. Bjorkholm, and S. Chu, "Observation of a Single-Beam Gradient Force Optical Trap for Dielectric Particles," Opt. Lett., Vol. 11, p. 288, 1986.

[37] A. Ashkin, "History of Optical Trapping and Manipulation of Small-Neutral Particles, Atoms, and Molecules," IEEE Journal on Selected Topics in Quantum Electronics, Vol. 6, p. 841, 2000.

[38] A. Ashkin, "Accelerating and Trapping of Particles by Radiation Pressure,". Phys. Rev. Lett., Vol 24, pp. 156-159, 1970.

[39] J. E. Molloy and M. Padgett, "Light, Action: Optical Tweezers", Contemporary Physics, Vol. 43, p. 241-258, 2002.

[40] P.Zemánek, V. Karasek, and M. Sery, "Behaviour of colloidal microparticles in a planar 3-beam interference field," Proc. SPIE 5514, p. 15–26, 2004.

[41] Y. Hayashi, S. Ashihara, T. Shimura, and K. Kuroda, "Particle Sorting Using Optically Induced Asymmetric Double-Well Potential," Opt. Commun., Vol. 281, pp 3792–3798, 2008.

[42] L. P. Faucheux, L. S. Bourdieu, P. D. Kaplan, and A. J. Libchaber, "Optical Thermal Ratchet", Phys. Rev. Lett., Vol. 74, p. 1504, 1995.

[43] M. P. MacDonald, G. C. Spalding, and K. Dholakia, "Microfluidic Sorting in an Optical Lattice," Nature, Vol. 426, p. 421-424, 2003.

[44] M. Pelton, K. Ladavac, and D. G. Grier, "Transport and Fractionation in periodic Potential Energy Landscapes," Phys. Rev.E. Vol. 70, 2004.

[45] F. C. Cheong, C. H. Sow, A. T. S. Wee, P. Shao, A. A. Bettiol, J. A. van Kan, and F. Watt, "Optical Travelator: Transport and Dynamic Sorting of Colloidal Microspheres with an Assymetrical Line Optical Tweezers," Appl. Phys. B-Lasers Opt., Vol 83, pp. 121-125, 2006.

[46] T. Cizmar, M. Siler, M. Sery, P. Zemánek, V. Garcés-Chávez, and K. Dholakia, "Optical Sorting and Detection of Sub-Micron Objects in a Motional Standing Wave," Phys. Rev., 2006.

[47] I. Perch-Nielsen, D. Palima, J. S. Dam, and J. Glückstad, "Parallel Particle Identification and Separation for Active Optical Sorting," J. Opt. A: Pure Appl. Opt., Vol. 11, 2009.

[48] F. Wyrowski and O. Brynghdahl, "Iterative Fourier Transform Algorithm Applied to Computer Holography," J. Opt. Soc. Am. A, Vol. 5, pp. 1058-1065, 1988.

[49] E. R. Dufresne, G. C. Spalding, M. T. Dearing, S. A. Sheets, and D. G. Grier, "Computer Generated Holographic Optical Tweezer Arrays," Rev. Sci. Instrum., Vol. 72, p. 1810, 2001.

[50] F. Wyrowski, "Diffractive Optical Elements: Iterative Calculation of Quantized Blazed Phase Structures," J. Opt. Soc. Am. A, Vol. 7, pp. 961-969, 1990.

[51] D. MacGloin and K. Dholakia, "Bessel Beams: Diffraction in a New Light", Contemp. Phys., Vol. 46, p. 15-28, 2005.

[52] J. Arlt, V. Garces-Chavez, W. Sibbett, and K. Dholakia, "Optical Micromanipulation Using a Bessel Light Beam," Opt. Commun. Vol. 197, pp. 239-245, 2001.

[53] L. Paterson, E. Papagiakoumou, G. Milne, V. Garces-Chavez, S. A. Tatarkova, and W. Sibbett, ". Light-Induced Cell Separation in a Tailored Optical Landscape," Appl. Phys. Lett., Vol. 87, 2005.

[54] I. Ricárdez-Vargas, P. Rodríguez-Montero, R. Ramos-García, and K. Volke-Sepúlveda, “A Modulated Optical Sieve for Sorting of Polydisperse Microparticles,” APPL. PHYS. LETT. 88, 121116 (2006).

[55] J. E. Curtis, B. A. Koss, and D. G. Grier, "Dynamic Holographic Optical Tweezers", Opt. Commun., Vol. 307, p. 169-175, 2002.

[56] R. L. Eriksen, V. R. Daria, and J. Gluckstad, "Fully Dynamical Multiple-Beam Optical Tweezers", Opt. Express, Vol. 10, p. 597-602, 2002.

[57] P. J. Rodrigo, V. R. Daria, and J. Gluckstad, "Dynamically Reconfigurable Optical Lattices", Opt. Express, Vol. 13, p.1384-1394, 2005.

[58] D. Palima, S. D. Jeppe, I. Perch-Nielsen, and J. Glückstad, “From Gaussian Beams to Optical Landscapes : Phase-Only Apertures Based on the Generalized Phase Contrast Method,” Proc. SPIE, Vol. 6905, 2008.

[59] B. A. Koss and D. G. Grier, "Optical Peristalsis", Appl. Phys. Lett., Vol. 82, p. 3985-3987, 2003.

[60] U. Ruiz, V. Arrizon, J. C. Ramirez, and R. Ramos, "Sorting of Microparticles by Optical Landscapes Generated with a Spatial Light Modulator," Proc. of SPIE, Vol. 7038, 2008.

[61] J. Rousselet, L. Salome, A. Ajdari, and J. Prost, "Directional Motion of Brownian Particles Induced by a Periodic Asymmetric Potential", Nature London, Vol. 370, p. 446, 1994.

[62] R. Krishnan, S. Roy, and A. M Jayannavar, “Enhanced Thermodynamic Efficiency in Time Asymmetric Ratchets” J. Stat. Mech., 2005.

[63] A.Ajdari and J. Prost, C.R. Acad. Sci. Paris II, Vol. 315, p. 1635, 1992.

[64] F. J. Cao, L. Dinis, and J. M. R. Parrondo, "Feedback Control in a Collective Flashing Ratchet", cond-mat., 2004.

[65] R.D. Astumian and M. Bier, Phys. Rev. Lett., Vol. 72, p. 1766, 1992.

[66] L. Gorre-Talini, J.P. Spatz, and P. Silberzan, “Dielectrophoretic Ratchets”, Chaos, Vol. 8, p. 650, 1998.

[67] V. Arrizón, D. Sánchez-de-la-Llave, U. Ruiz, and G. Méndez, "Efficient Generation of an Arbitrary Nondiffracting Bessel Beam Employing its Phase Modulation," Opt. Lett., Vol. 34, pp. 1456-1458, 2009.

[68] V. Arrizón, U. Ruiz, G. Mendez, and A. Apolinar, "Zero Order Synthetic Hologram with a Sinusoidal Phase Carrier for Generation of Multiple Beams," Opt. Express, Vol.17, pp. 2663-2669, 2009.